ceramics

MDPI

Article

Enhancing Dielectric, Electrical, and Gas Sensing Properties of $CaFeO_{3-\delta}$ Through Sintering Temperature Optimization

Amina Benatia [1,*], Najwa Gouitaa [1], Ina Turcan [2,3], Felicia Gheorghiu [4], Laura-Elena Ursu [5], Liviu Leontie [6,*], Liliana Mitoseriu [3], Fatima Zahra Ahjyaje [1], Taj-dine Lamcharfi [1] and Farid Abdi [1]

1 Signals, Systems and Components Laboratory, Faculty of Science and Technology of Fez, University Sidi Mohammed Ben Abdellah USMBA, Route d'Imouzzer, Fez P.O. Box 2202, Morocco
2 "Ion Ionescu de la Brad" Iasi University of Life Sciences, 3 Mihail Sadoveanu Alley, 700490 Iasi, Romania
3 Dielectrics, Ferroelectrics & Multiferroics Group, Faculty of Physics, Alexandru Ioan Cuza University of Iasi, 11 Carol I Blvd., 700506 Iasi, Romania
4 Ramtech Center, Department of Exact & Natural Sciences, Institute of Interdisciplinary Research, Alexandru Ioan Cuza University of Iasi, 11 Carol I Blvd., 700506 Iasi, Romania
5 Petru Poni Institute of Macromolecular Chemistry, Romanian Academy, Grigore Ghica Voda Alley, 41A, 700487 Iasi, Romania
6 Faculty of Physics, Alexandru Ioan Cuza University of Iasi, 11 Carol I Blvd., 700506 Iasi, Romania
* Correspondence: amina.benatia@usmba.ac.ma (A.B.); lleontie@uaic.ro (L.L.)

Abstract

This research aims to investigate the modifications of the structural, dielectric, and sensing properties of $CaFeO_{3-\delta}$ ceramics produced by solid-state reaction induced by varying sintering temperatures in the range of 1000–1200 °C. A single crystallographic orthorhombic (Pcmn) structure was revealed by X-ray diffraction with Rietveld analysis, both for the powders and sintered ceramics, irrespective of the sintering temperature. The increase in the sintering temperature induces better densification and a larger grain size. Dielectric measurements reveal a pronounced enhancement of the relative permittivity, reaching 2×10^5 at 1 kHz and 330 °C for the sample sintered at 1200 °C/4 h. This composition also displays the highest electrical conductivity, 0.4 S/m at 1 MHz. Cole–Cole analysis indicates a clear deviation from ideal Debye behavior, while the relaxational features of the dielectric permittivity suggest a strong correlation between the dielectric response and Fe-related conduction mechanisms. Gas sensing tests show that the ferrite ceramics exhibit consistent ethanol response trends. The ceramic sintered at 1200 °C/4 h achieved the highest sensitivity, of 56.28%, which can be attributed to its higher density, larger ceramic grains, and reduced low-frequency conductivity. The $CaFeO_{3-\delta}$ ceramic sintered at 1200 °C/4 h shows a combination of high permittivity, enhanced conductivity, and strong ethanol sensitivity, making it a promising material for dielectric components, capacitive devices, and gas sensing applications.

Keywords: $CaFeO_{3-\delta}$; sintering temperature; dielectric properties; electrical conductivity; ethanol sensing

Academic Editors: Dawei Wang, Raz Muhammad, Zhilun Lu and Fangfang Zeng

Received: 3 February 2026
Revised: 10 March 2026
Accepted: 13 March 2026
Published: 17 March 2026

1. Introduction

In recent years, the need for efficient gas sensors has become increasingly urgent due to growing concerns over environmental pollution [1], industrial safety, and public health [2]. Applications such as air quality monitoring, chemical process control, and medical diagnostics rely heavily on sensitive, selective, and stable sensors to detect trace amounts of hazardous gases [3]. Traditionally, metal oxide semiconductors like SnO_2, ZnO,

and Fe_2O_3 have been widely employed since the 1960s for this purpose [2,4]. Moreover, functional oxides beyond conventional binary MOS have been proposed for specific targets, for example, ZrO_2-based materials for oxygen sensing (via oxygen-vacancy-related mechanisms) [5] and spinel MgO–Al_2O_3 ceramics for humidity sensing due to their porous microstructure and stability [6].

While these materials offer acceptable sensitivity, they often suffer from some limitations, such as poor selectivity, signal drift over time, and instability in humid environments. To overcome the limitations of classical metal oxide sensors, recent research has focused on more complex oxides—particularly ferrite-based perovskites, which possess multiferroic properties, a high concentration of oxygen vacancies, and semiconductivity. Materials such as $BiFeO_3$, $LaFeO_3$, and $GdFeO_3$ have shown enhanced stability and sensitivity in various gas sensing applications [7,8]. Ferrites have demonstrated reliable detection of a wide range of gases, including volatile organic compounds (VOCs) like methanol [9], ethanol [4], acetone [10,11], methane, NH_3 [12], CO, CO_2 [13], and hydrogen [2]. Their low cost, suitability for low-temperature operation, and potential for tunable performance through doping and synthesis optimization make them highly attractive for next-generation gas sensors [7,14,15]. In this context, several recent studies have emphasized the ethanol-sensing potential of doped or surface-modified ferrite perovskites. For instance, H. Xu et al. found that Sr-doped $BiFeO_3$ exhibited a response of ~49.5% to ethanol at 208 °C, outperforming undoped $BiFeO_3$ [16,17]. Similarly, Yang Chen et al. reported a sensitivity of 50.6 to ethanol at 180 °C using Ag-$LaFeO_3$ nanosheets, with fast response and recovery times [18]. Within this broader class of materials, calcium ferrite ($CaFeO_{3-\delta}$) stands out due to its structural flexibility, mixed ionic–electronic conduction, and naturally occurring oxygen non-stoichiometry [19]. These features create abundant active sites for gas adsorption and facilitate charge transfer processes. In addition to sensing, $CaFeO_{3-\delta}$ adopts an orthorhombic perovskite structure (space group Pcmn), consisting of a three-dimensional framework of corner-shared FeO_6 octahedra [20,21]. Its structure naturally accommodates oxygen vacancies (δ), which serve as active sites for gas adsorption and facilitate charge transfer processes [22,23]. These vacancies, along with the mixed valence states of iron (Fe^{3+}/Fe^{4+}) [24,25], not only influence magnetic behavior—shifting from G-type antiferromagnetism in the stoichiometric phase to room-temperature ferromagnetism in oxygen-deficient compositions, but also contribute significantly to the material's mixed ionic–electronic conductivity [26]. Given its redox-active iron centers and oxygen-deficient structure, $CaFeO_{3-\delta}$ is expected to exhibit sensitivity toward reducing gases like ethanol, an area that has yet to be thoroughly investigated. In addition to sensing, $CaFeO_{3-\delta}$ exhibits promising dielectric characteristics, such as a colossal dielectric constant (~10^5) near its transition temperature (257 °C), which is strongly dependent on grain size effects and frequency [20,27]. Such features make it a candidate not only for gas sensors but also for use in capacitors and other microelectronic components [19]. Despite extensive studies on the magnetic and catalytic properties of $CaFeO_{3-\delta}$, the effect of sintering temperature on its dielectric, electrical, and sensing properties remains largely unexplored. In particular, the relationship between sintering-induced microstructural changes and multifunctional performance has not been systematically investigated.

In this work, we investigated how different sintering temperatures affect the structural, dielectric, electrical, and gas sensing properties of $CaFeO_{3-\delta}$ ceramics prepared via solid-state synthesis. Specifically, we aimed to elucidate how the sintering temperature governs the phase formation, porosity, and grain size; to clarify how these microstructural changes modify the dielectric response and the related grain and grain-boundary conduction mechanisms; and to evaluate their impact on the ethanol sensing, stability, and response recovery behavior.

2. Materials and Methods

As schematically shown in Figure 1, the $CaFeO_{3-\delta}$ powders are produced by the solid-state technique, by mixing stoichiometric quantities of calcium carbonate (99.9 atom%, Sigma-Aldrich (St. Louis, MO, USA)) and iron oxide (99.9 atom%, Sigma-Aldrich (St. Louis, MO, USA)) dried powders, following the standard chemical Equation (1):

$$CaCO_3 + \frac{1}{2}Fe_2O_3 \rightarrow CaFeO_{3-\delta} + CO_2 \uparrow \quad (1)$$

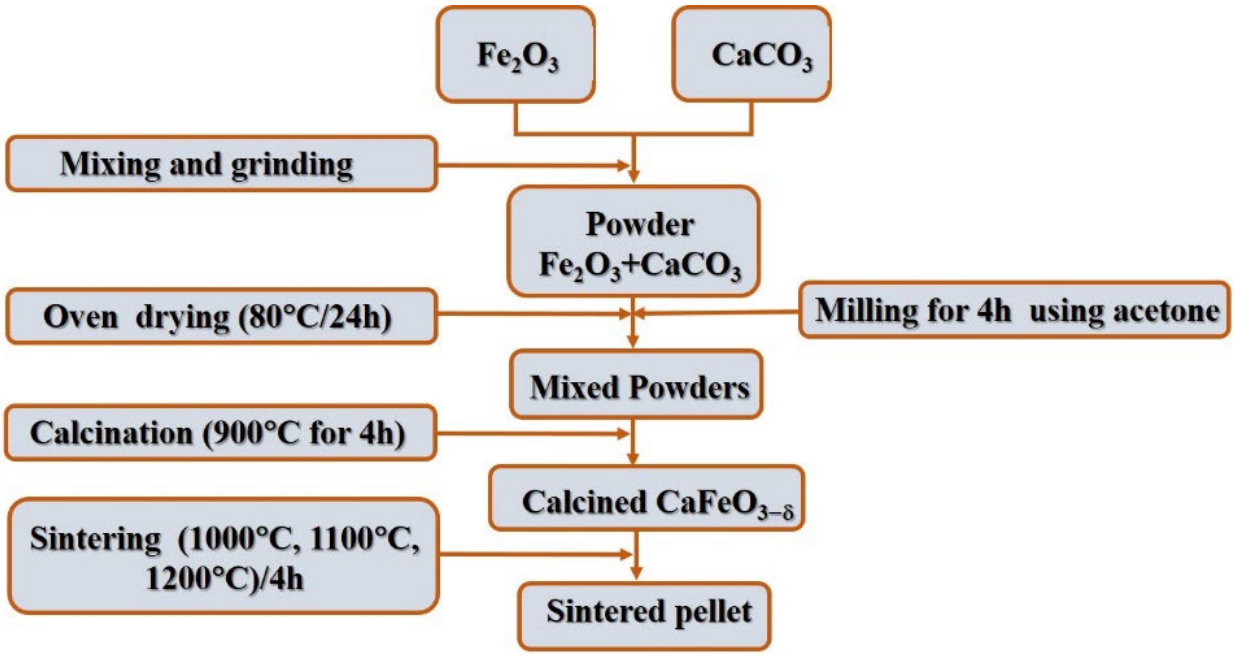

Figure 1. Schematic representation of the processing steps involved in the preparation of $CaFeO_{3-\delta}$ ceramics by solid-state route.

These ceramics were crushed in an agate mortar and homogenized by grinding under acetone before the calcination step at 900 °C for 4 h in ambient air. The calcined powders were combined with a (PVA) polyvinyl alcohol binder solution after being ground. In order to obtain pellets (thickness ≈ 1/2 mm and diameter ≈ 12 mm) for the dielectric and electric measurements, the powders were compressed under 8 tons by a hydraulic press (Specac Ltd., Orpington, UK) Finally, they were sintered in ambient air at variable temperatures (1000 °C, 1100 °C, and 1200 °C) for 4 h, with a controlled heating rate of 3 °C/min in a programmable furnace (Nabertherm GmbH, Lilienthal, Germany).

The sintering condition effect on the structural properties of $CaFeO_{3-\delta}$ was analyzed by X-ray diffraction XRD (XPERT-PRO with CuK radiation (λ = 1.5405 nm, 2θ∼20–80° with a scanning rate of 0.02°/s). The FULLPROF (ILL/CNRS, Grenoble, France; FullProf version 2023) suite software was used for Rietveld refinement, to identify the crystalline phase, and to determine the lattice parameters. Scanning electron microscopy was utilized to examine the microstructure of the resulting pellets. SEM/EDX analyses were carried out using FEI Quanta 200 coupled with EDX systems (FEI Company, Hillsboro, OR, USA). Samples were mechanically ground/polished (SiC P320–P1200; diamond 6–1 µm), cleaned with ethanol, and coated with a conductive layer (<10 nm; Au/Pt/C depending on imaging/EDX) to minimize charging; measurements were performed at 5–15 kV with ~8–10 mm working distance. To create a planar capacitor, a fine coating of silver paste was applied to the sides of the pellets after sintering. The dielectric properties as a function of frequency (1000 Hz–2 MHz) and temperature (40–500 °C) were obtained by using an LCR meter

(Agilent HP4284A, Agilent Technologies, Santa Clara, CA, USA) operated under 1 V. Additionally, electrical conductivity is an indicator of a substance's degree of charge mobility. Using the obtained dielectric measurements and Equation (2), the AC conductivity σ_{ac} was also determined:

$$\sigma_{ac} = \omega\ \varepsilon_r\ \varepsilon_0\ tan\delta, \quad (2)$$

where ω is the angular velocity, ε_r and ε_0 are the relative permittivity of the material and vacuum, respectively, and tanδ gives the dielectric loss. To study the electrical behavior of ceramics, complex impedance spectroscopy technology was exploited [28]. In the case of $CaFeO_{3-\delta}$ ceramics, the impedance elements are usually represented by an equivalent circuit which is derived from the resistance–capacitance (RC) model, which is adapted to describe the electrical behavior of all the ceramic contributions (the grains (R_g, C_g) and grain boundaries (R_{gb}, C_{gb}), characterized by different electrical properties [29]. The complex impedance responses of the entire ceramic sample are described by the equation [30]:

$$Z' = \left(R_g^{-1} + j\omega C_g\right)^{-1} + \left(R_{gb}^{-1} + j\omega C_{gb}\right)^{-1} \quad (3)$$

The ethanol-sensing responses were evaluated by impedance spectroscopy Hameg HM8118 Programmable LCR Bridge (HAMEG GmbH, Frankfurt, Germany), operating at room temperature and atmospheric pressure. Sensing tests were performed in a 200 mL sealed static chamber using an open ethanol reservoir to generate near-saturated vapor at 25 °C (ambient conditions). As the ethanol concentration was not controlled in ppm, the sensing results are discussed as qualitative comparisons among sintering conditions. The complex impedance of the ceramic samples was recorded under an alternating voltage of 1 V at different frequencies (1 kHz, 5 kHz, and 10 kHz), first in ambient air and then in a saturated ethanol atmosphere. The detection procedure consisted of several exposure–recovery cycles by alternately placing the samples in open air and ethanol vapors, in order to assess the sensing repeatability.

3. Results and Discussions

3.1. X-Ray Diffraction Analyses

X-ray diffraction (XRD) analysis, as shown in Figure 2, was carried out to examine the phase evolution and structural crystallinity of $CaFeO_{3-\delta}$ powders sintered at 1000 °C, 1100 °C, and 1200 °C for 4 h. All the diffractograms display sharp and well-defined diffraction peaks corresponding to the orthorhombic perovskite structure, confirming the successful formation of the $CaFeO_{3-\delta}$ phase. No secondary phases were detected within the resolution limits of the XRD, indicating high phase purity under the chosen sintering conditions. Furthermore, the observed diffraction patterns are in good agreement with the standard JCPDS card No. 41-0753 [31], consistent with previous findings reported in ref. [19]. Rietveld refinement performed using FULLPROF software (version 2023) (Figure 3) confirmed that all the samples crystallize in an orthorhombic structure with the Pcmn space group, consistent with previous findings in ref. [32]. Notably, the diffraction peak at 2θ~35.53° (indexed as the (211) plane of the $CaFeO_{3-\delta}$ Pcmn phase) decreases in normalized intensity with increasing sintering temperature. The reduced (211) peak intensity is discussed mainly in terms of preferred orientation and intensity redistribution during sintering. This interpretation is supported by the strong decrease in I_{211}/I_{max} (0.11366 → 0.04711 → 0.01426), whereas the FWHM (211) does not decrease with sintering temperature (0.118° → 0.139° → 0.143°) (Table 1) [33,34]. The refinement results provided key structural parameters, including the reliability factor (χ^2), unit cell volume (V), and lattice constants a, b, and c, which are summarized in Table 1. These lattice constants show a non-linear trend with increasing sintering temperature, which can arise from coupled

effects such as microstrain relaxation, subtle changes in oxygen non-stoichiometry (δ) and Fe valence balance, and anisotropic lattice response in orthorhombic perovskites, rather than necessarily implying cation disorder [35]. Additional factors such as surface energy, internal stress, and grain-boundary deformation [36] may also influence these variations. Slight shifts in lattice parameters could alter Fe–O–Fe bond angles and hopping distances, which are important for polaron hopping and charge transport in $CaFeO_{3-\delta}$. Furthermore, a small increase in the unit cell volume at higher temperatures may reflect a rise in the oxygen-vacancy concentration. The goodness-of-fit values, with χ^2 ranging from 1 to 2 and refinement factors Rp $\leq$ 6% and Rwp $\leq$ 9%, confirm the high quality of the structural refinement across all samples.

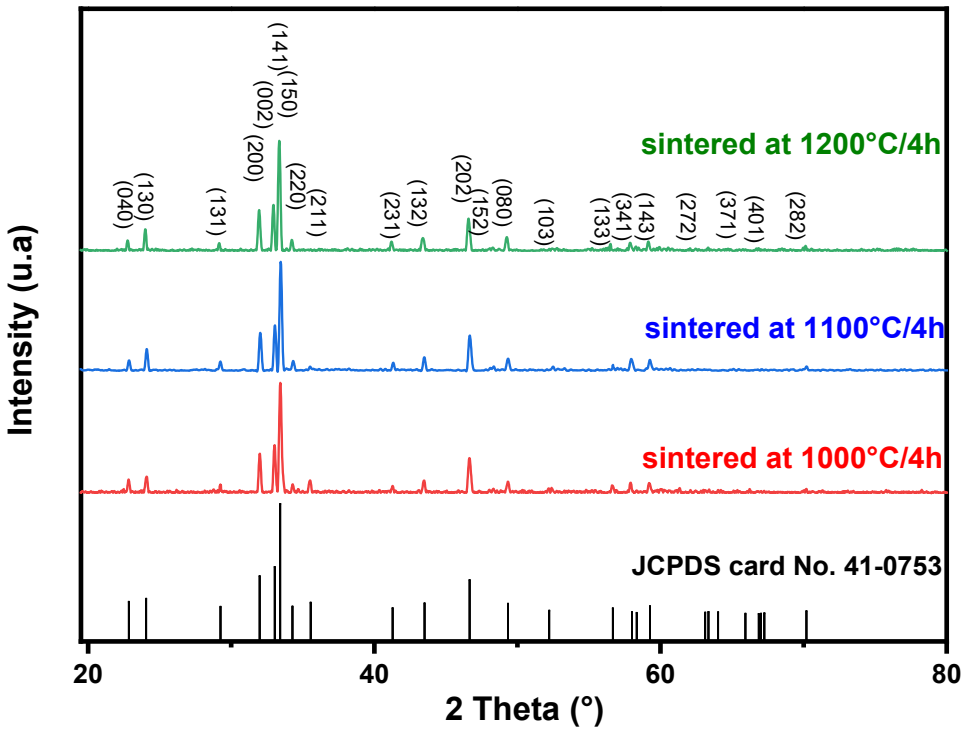

Figure 2. Characterization by XRD of $CaFeO_{3-\delta}$ samples sintered at different temperatures.

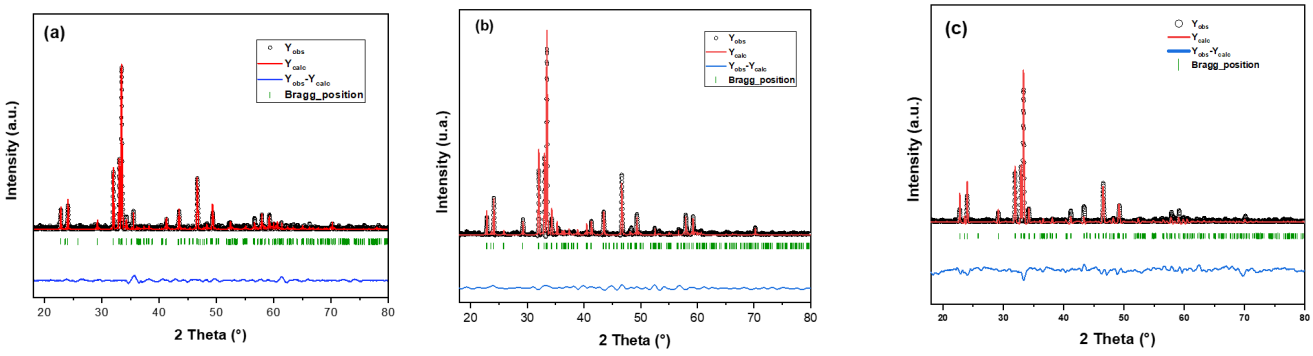

Figure 3. The fit obtained by the FULLPROF program using the Rietveld method for ceramic sintered at: (**a**) 1000 °C/4 h, (**b**) 1100 °C/4 h, (**c**) 1200 °C/4 h.

Table 1 shows the width of the diffraction peaks (FWHM) and the average size of the crystallites as a function of the heat treatment. This indicates that the prepared materials have a nanocrystalline nature. The average crystallite size was calculated using the Scherrer method [35], as per Equation (4):

$$D = \frac{K\gamma}{\beta \cos\theta}, \quad (4)$$

where γ is the X-ray wavelength of the Cu Kα source (0.154050 nm), β: full width at half intensity (FWHM), D: average grain size, and θ: Bragg diffraction angle. As expected, the crystallite size increases with rising sintering temperature, as found in previous reports [37,38]. This trend is attributed to enhanced grain growth at higher temperatures, which reduces the density of grain boundaries and thus may improve charge carrier mobility by minimizing scattering. Similar behavior has been observed in ref. [39] for $LaFeO_3$-based materials, reinforcing the correlation between thermal treatment and microstructural development.

Table 1. Parameters (a, b, and c) derived from the Rietveld fit and crystallite size, FWHM (211), and I_{211}/I_{max} for all the ceramics.

Samples	a (A°)	b (A°)	c (A°)	V (A°)^3	Reliability Factors	Crystallite Size D (nm)	FWHM (211)	I_{211}/Imax
Sintered at 1000 °C/4 h	5.61	14.77	5.37	446.41	χ^2: 1.63 Rp: 4.05% Rwp: 5.12%	43.711	0.118	0.113
Sintered at 1100 °C/4 h	5.58	14.76	5.41	447.16	χ^2: 1.36 Rp: 4.94% Rwp: 6.10%	45.772	0.139	0.047
Sintered at 1200 °C/4 h	5.60	14.83	5.39	448.84	χ^2: 1.53 Rp: 5.95% Rwp: 7.28%	47.492	0.143	0.014

3.2. Raman Spectroscopy Analysis

Figure 4 presents the Raman spectra of $CaFeO_{3-\delta}$ pellets sintered at various temperatures. All the ceramic samples display the characteristic vibrational modes of the orthorhombic perovskite structure, with a clear progressive narrowing of the bands and an increase in the peak intensity as the sintering temperature rises. These spectral changes indicate an improved crystallinity, reduced local structural disorder and improved lattice coherence, and enhanced long-range order of the FeO_6 octahedral network when using higher sintering temperatures [40]. In the low-frequency region (≈250–305 cm^{-1}), the observed bands are associated with A-site cation motions and lattice bending modes, consistent with previous perovskite assignments. The mode near 375 cm^{-1} corresponds to mixed Ca–O vibrations [41], while intermediate modes around 375–425 cm^{-1} can also be linked to Fe–O bending within FeO_6 octahedra. Fe–O stretching vibrations dominate the higher-frequency region (≈550–707 cm^{-1}). Among these, the symmetric stretching mode near 707 cm^{-1} is attributed to the breathing-type distortion of FeO_6 octahedra [39]. A band around 667 cm^{-1} is assigned to Fe–O stretching vibrations associated with FeO_6 octahedral distortion and local symmetry breaking within the perovskite lattice, as reported by Weber et al. and Islam et al. [42,43]. The most pronounced changes with increasing temperature occur in the Fe–O stretching modes (notably at 667 and 707 cm^{-1}): The full width at half-maximum (FWHM) decreases, and the peak intensity increases significantly. These changes reflect a more ordered FeO_6 framework and a lower degree of local distortion/defect-related broadening in the ceramics sintered at higher temperatures. Conversely, at 1000 °C, the broader, weaker bands indicate higher defect levels, greater oxygen non-stoichiometry (δ) contribution, and less ordered FeO_6 connectivity. Overall, the Raman spectra are consistent with previous reports, confirming that the CFO ceramics maintain a well-ordered orthorhombic perovskite structure [44].

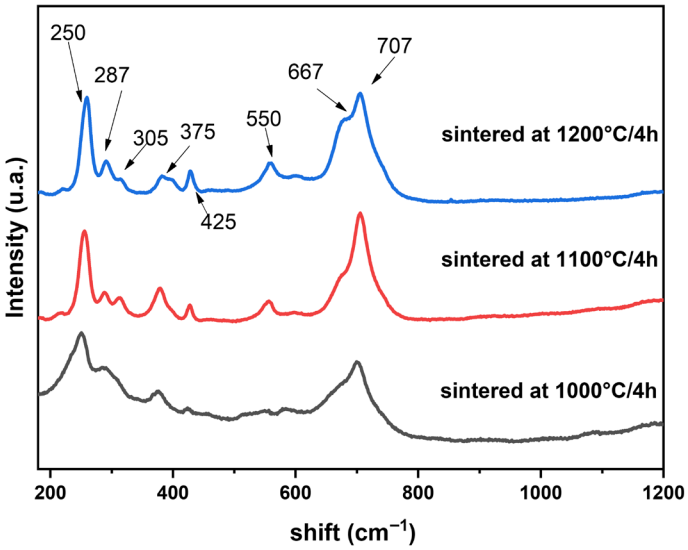

Figure 4. Characterization by Raman of $CaFeO_{3-\delta}$ samples sintered at different temperatures.

3.3. Microstructural Characterization

The evolution of the morphology and grain size of $CaFeO_{3-\delta}$ ceramic as a function of different sintering temperatures was studied by using scanning electronic microscopy SEM and is shown in Figure 5. SEM micrographs present a combination of small and large grains for each sample, revealing a size heterogeneity. The samples sintered at (1000–1100 °C/4 h) show significant porosity and agglomeration with a variation in morphology and grain size. At higher sintering temperatures (1200 °C/4 h), the agglomeration and porosity phenomenon decrease [45], and the surface becomes flat, with a regular ceramic grain arrangement, typical for the sintered ceramics with well-connected grains and with typical of well-sintered ceramics with improved grain-to-grain connectivity. These observations indicate enhanced densification and microstructural homogenization at higher sintering temperatures [46]. The same approach was found for the perovskite $LaFeO_3$ formed by the sol–gel reaction and in refs. [35,47]. The mean grain size estimated from the particle size distribution histogram confirms that the high-temperature sintered sample (~1200 °C/4 h) has a larger particle size. Based on the EDS analyses, the sample of $CaFeO_{3-\delta}$ contains Ca, Fe, and O elements, along with some impurities of C. According to Table 2, the ratio Ca/Fe is around 1:1, corresponding with the expected stoichiometry range, by accounting for errors in the experiments. A measurable carbon (C) signal is also present and decreases with sintering temperature (≈6.8 → 5.8 → 1.9 wt% at 1000/1100/1200 °C; Table 2). Since EDS is surface-sensitive, this signal can partly be attributed to the thin conductive carbon coating applied prior to SEM/EDS measurements to reduce surface charging [48], in addition to possible surface carbonation/adventitious carbon. Therefore, the EDS carbon content is not interpreted as a direct quantitative proof of bulk residual binder. Nevertheless, during air sintering, the decomposition of any remaining organics can generate CO/CO_2; if densification proceeds simultaneously, gas evacuation becomes limited, and a fraction of porosity may evolve toward closed pores. This interpretation is consistent with the strong densification measured by the Archimedes method (Table 3: 69% → 90% → 92%), indicating reduced open porosity and possible pore closure at advanced sintering stages [47].

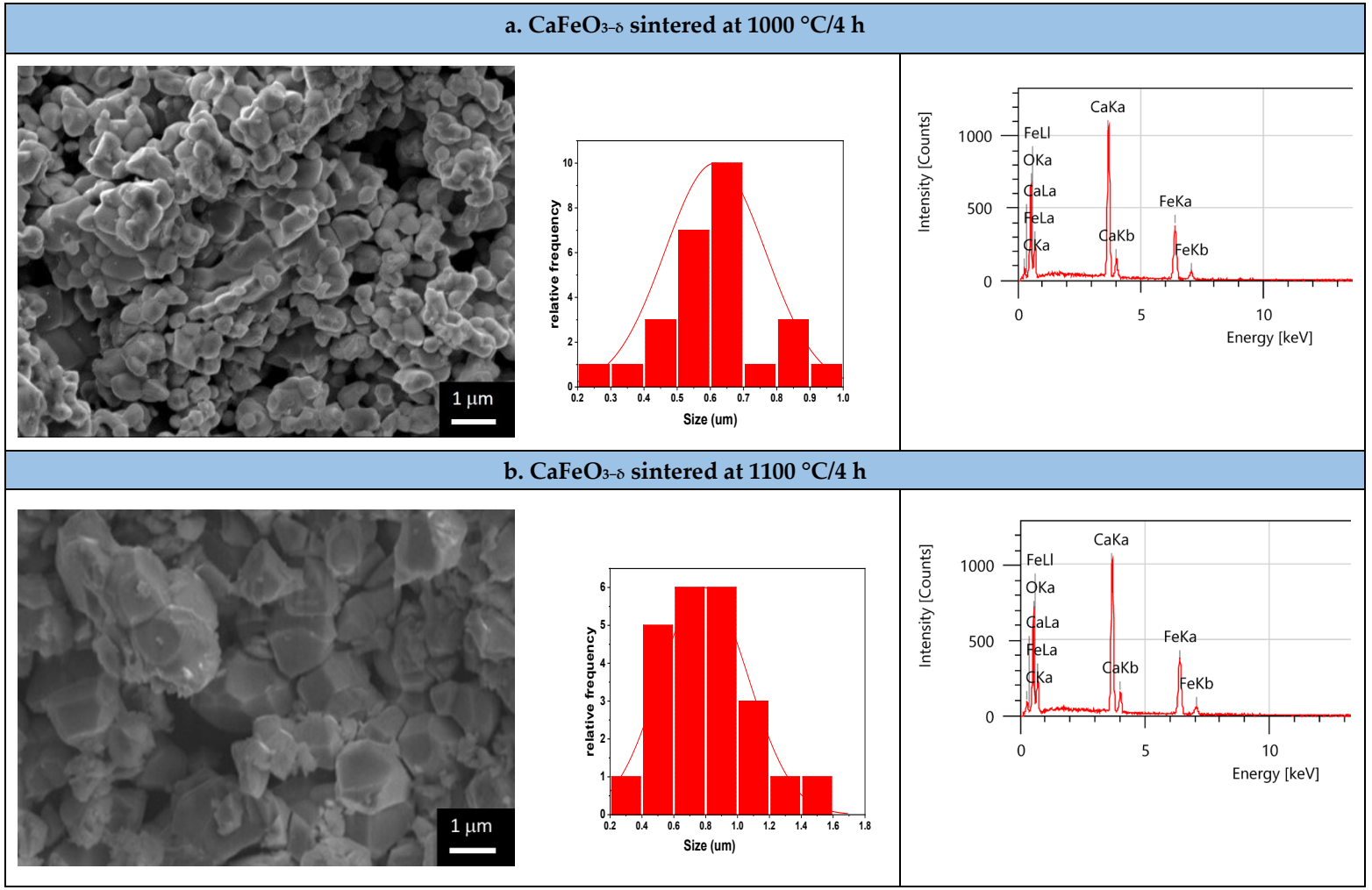

Figure 5. *Cont.*

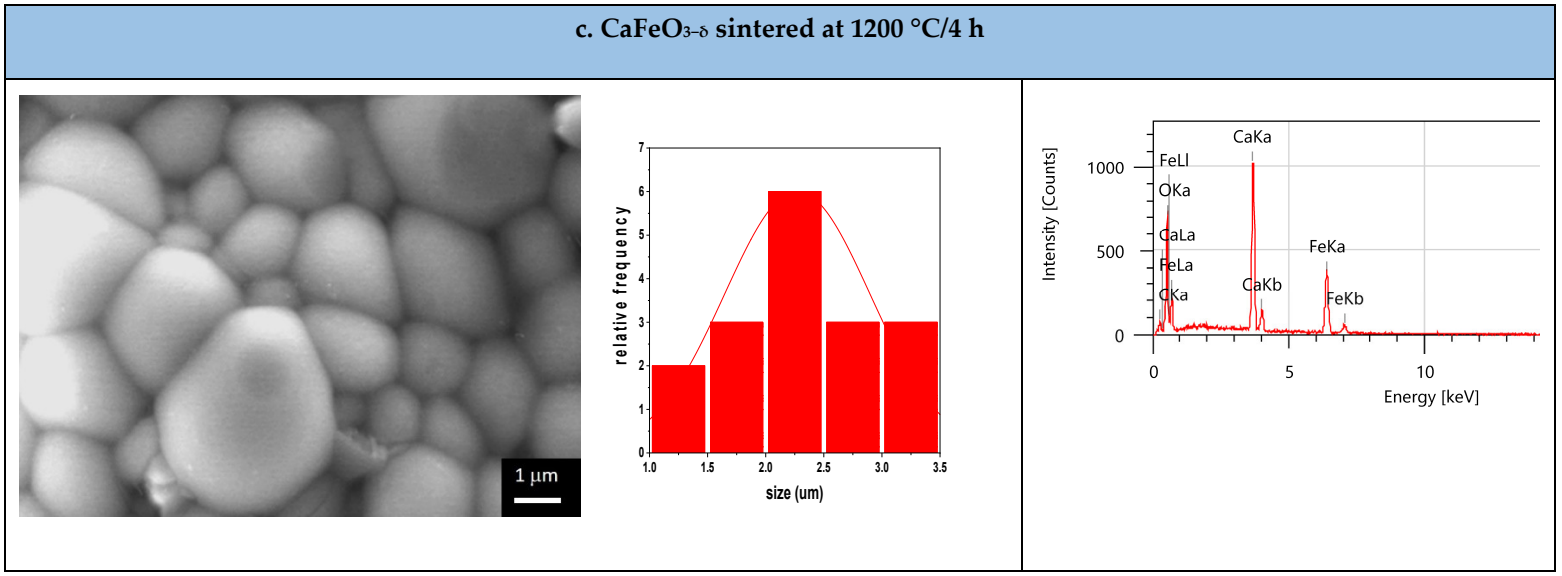

Figure 5. SEM images, particle size distribution histogram, and EDS graphs of $CaFeO_{3-\delta}$ pellets sintered at different temperatures.

Table 2. Weight and atom percentage of all elements for all the ceramic samples.

Elements	Weight%	Atom%	Weight%	Atom%	Weight%	Atom%	Weight %	Atom%
	C (K)		O (K)		Ca (K)		Fe (K)	
Sintered at 1000 °C/4 h	6.77 ± 0.01	15.09 ± 0.02	21.96 ± 0.05	41.20 ± 0.05	29.87 ± 0.04	22.88 ± 0.02	41.40 ± 0.08	22.04 ± 0.04
Sintered at 11000 °C/4 h	5.75 ± 0.01	14.07 ± 0.03	22.98 ± 0.05	42.22 ± 0.05	29.97 ± 0.05	21.98 ± 0.03	41.30 ± 0.09	21.74 ± 0.05
Sintered at 1200 °C/4 h	1.86 ± 0.05	4.71 ± 0.01	26.03 ± 0.03	49.55 ± 0.04	29.95 ± 0.03	22.75 ± 0.02	42.16 ± 0.06	22.99 ± 0.03

Table 3. Density (Archimedes method), average grain size, and the permittivity maximum at 1 KHz for all the $CaFeO_{3-\delta}$ ceramics sintered at different temperatures.

Samples Sintered at:	Density (%)	Grain Size (μm)	Permittivity ε_r (1 kHz)
1000 °C/4 h	69	0.14	25,124
1100 °C/4 h	90	0.89	5553
1200 °C/4 h	92	2.32	216,113

3.4. Dielectric Properties

Figure 6 presents the temperature dependence of the dielectric permittivity of $CaFeO_{3-\delta}$ ceramics sintered at temperatures ranging from 1000 °C to 1200 °C for 4 h. As depicted in Figure 6a, the 1000–1100 °C pellets exhibit two permittivity maxima (T_1, T_2). The one corresponding to the temperature T_1 = 241 °C is attributed to an extrinsic Maxwell–Wagner/IBLC relaxation produced by semiconducting grains separated by more resistive grain boundaries; its strong frequency dispersion and sensitivity to densification are classical fingerprints of a grain-boundary-dominated response in polycrystalline perovskites. By contrast, the higher-temperature maximum at the temperature T_2 = 280 °C is assigned to an intrinsic bulk relaxation linked to small polaron/defect-dipole dynamics on the Fe^{3+}/Fe^{4+}–O network in the presence of oxygen vacancies (δ). Because $CaFeO_{3-\delta}$ is an oxygen-nonstoichiometric ferrite, the oxygen-vacancy concentration (δ) and the Fe^{3+}/Fe^{4+} ratio are thermodynamically dependent on temperature and oxygen partial pressure. In Fe-based perovskites, variations in δ are charge-compensated by changes in iron valence, which directly affect polaron hopping and dipolar defect dynamics. Consequently, differences in sintering temperature and the associated defect equilibration during heating and cooling in air are expected to influence δ and the Fe^{3+}/Fe^{4+} balance, thereby modulating the dielectric relaxation behavior. In the present work, δ and Fe valence were not directly quantified; therefore, this interpretation is proposed as a literature-supported mechanism consistent with the observed dielectric and impedance trend [49,50]. With densification and grain growth, the contribution of interfacial polarization can be reduced/shifted, leading to a simplified relaxation behavior; this remains consistent with a grain/GB heterogeneous (Maxwell–Wagner/IBLC-type) framework. In contrast, sintering at 1200 °C significantly enhances the diffusion, leading to grain coarsening and improved densification (SEM and Archimedes, Table 3, ~92% relative density). The reduction in grain-boundary area diminishes the influence of interfacial polarization and favors a single broad bulk relaxation (Figure 6b) [45]. The pronounced dielectric response observed in the sample sintered at 1200 °C, with a colossal permittivity reaching approximately 2.1×10^5 (at 1 kHz and 330 °C), can be explained by the internal barrier layer capacitor (IBLC) model [34,35]. According to this model, the effective dielectric constant (ε_r) depends on the grain-boundary dielectric

constant (ε_{gb}), average grain size (A), and grain-boundary thickness (t), expressed via a specific Equation (5):

$$\varepsilon_r = \varepsilon_{gb} \frac{A}{t}, \quad (5)$$

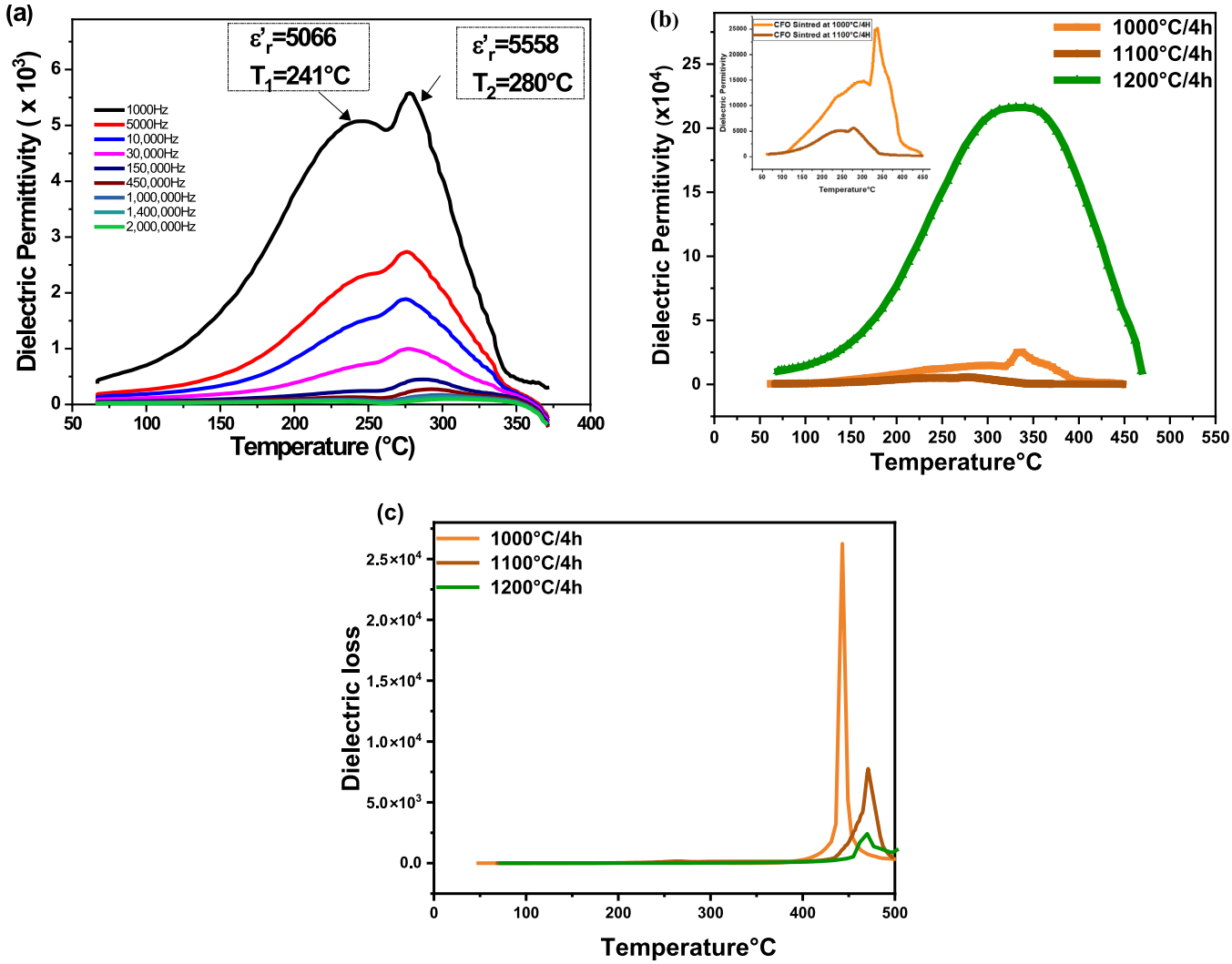

Figure 6. Dielectric properties of the $CaFeO_{3-\delta}$ ceramic sample sintered at different temperatures: (**a**) permittivity as a function of temperature at different frequencies (1000–2 × 10^6 Hz) for the ceramic sintered at 1100 °C/4 h; (**b**) permittivity as a function of temperature at 1 kHz for all the $CaFeO_{3-\delta}$ ceramics; (**c**) the dielectric loss as a function of temperature at 1 kHz for all the $CaFeO_{3-\delta}$ ceramics.

Since the sample sintered at 1200 °C possesses the largest average grain size (~2.32 µm), its properties are related to a reduction in grain-boundary density. The grain boundaries hinder the charge transport and serve as sites for the dielectric relaxation; their reduction causes the enhancement of charge mobility and polarization efficiency. The same relationship was observed by V.R. Mudinepalli [51]. This high dielectric permittivity can be compared to that observed in $CaTiO_3$-$FeTiO_3$ composites [52] and in $CaCuTi_4O_{12}$ ceramics [53]. Additionally, the increased densification achieved at higher sintering temperature reduces porosity and improves grain-to-grain connectivity, thereby lowering interfacial barrier effects and diminishing Maxwell–Wagner-type polarization associated with electrical heterogeneity (grain boundaries/pores/electrode interfaces) [51]. Consequently, the dielectric permittivity increases markedly with sintering temperature, along with a significant decrease in the dielectric loss. As shown in (Figure 6c), the samples exhibit a low dielectric loss tangent from ambient temperature up to 400 °C. However, above ~400 °C,

samples sintered at 1000 °C and 1100 °C display sharp loss peaks, which can be attributed to Maxwell–Wagner interfacial polarization and the thermally activated movement of space charges and oxygen vacancies at porous grain boundaries. These defects, commonly found in poorly densified ceramics, promote leakage conduction and energy dissipation at higher temperatures. In contrast, the sample sintered at 1200 °C shows a much lower, broader tan δ peak, indicating suppressed dielectric loss due to improved densification, larger grains, and fewer grain boundaries. This implies more stable dielectric behavior governed by intrinsic lattice polarization rather than defect-related conduction [54]. Overall, by increasing the sintering temperature, dielectric losses are significantly reduced by limiting oxygen-vacancy relaxation processes and by enhancing grain connectivity [55]. These results highlight the importance of controlled grain growth and defect engineering achieved by increasing the sintering temperature in obtaining high dielectric performances of $CaFeO_{3-\delta}$ ceramics.

The permittivity variation with frequency for all the samples is displayed in Figure 7. As observed, the permittivity values strongly reduce from giant values (from 2×10^3 to 18×10^3 at 10^3 Hz) in the low field range, until reaching low values of units at high frequencies (i.e., in the range of 15–37 at 2×10^6 Hz). Only the high-frequency stabilized permittivity value can be considered as an intrinsic value for this compound, while at low frequencies, extrinsic contributions contribute strongly to increasing the total polarization and permittivity [56,57]. The low-frequency permittivity values are connected to the polarization caused by space charge and the alteration of cation valence states [58]. The enhanced conduction in these samples, or the electron hopping process, generates electron polarization and contributes to dispersion in the low-frequency region, thus explaining the significantly high value of permittivity [59,60]. In agreement with the Maxwell–Wagner [61] kind of interfacial polarization, Koop's theory [62] can also explain this observed behavior. As a result of the existence of Fe^{3+}/Fe^{2+} ions, the ceramic polarization is associated with the dipoles of the ferrite phase. Nevertheless, an orientational polarization is produced by the electron transfer between the $Fe^{2+} \leftrightarrow Fe^{3+}$ dipoles, which aligns the dipoles with the AC applied alternating field. In the higher-frequency range, the permittivity is almost frequency-independent, due to the electron exchange between $Fe^{2+} \leftrightarrow Fe^{3+}$, which are unable to follow the alternating field AC at such high frequencies [55].

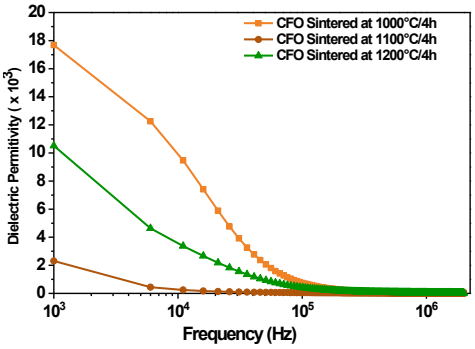

Figure 7. The permittivity as a function of frequency at ambient temperature for the $CaFeO_{3-\delta}$ ceramics sintered at different temperatures.

3.5. Electric Properties

To illustrate the impact of sintering temperature on the ceramic electrical conductivity (σ), we examined the conductivity in a frequency range (1 kHz–1 MHz). Figure 8 illustrates the conductivity evolution for all the samples at 310 °C. The conductivity (σ) rises with increasing frequency, but becomes stable irrespective of the frequency in low-frequency regions, and tends to saturate to a value known as the DC conductivity (σ_{DC}) [63]. This low-frequency plateau corresponds to the dc component σ_{DC}, while the high-frequency

dispersion reflects localized AC transport, attributed to localized transport or hopping of charge carriers [61]. As observed in Figure 8, the DC conductivity reduces by about one order of magnitude, from 2.6 × 10^{-2} S/m for the ceramic sintered at 1000 °C to 5.3 × 10^{-3} S/m for the ceramic sintered at 1100 °C, and remains the same when the sintering temperature is raised to 1200 °C. But the overall AC conductivity of this ceramic increases strongly with frequency, meaning that, for the dense ceramic with larger grains, other AC conduction mechanisms may become active at high temperatures [64]. Usually, at high frequencies, conductivity increases due to the small polaron hopping mechanism [65]. These dependences demonstrate the existence of small polaron in this solid material, thus contributing to enhancing their AC conductivity (σ_{AC}). In line with Koop's model and Maxwell–Wagner's theory, conductive iron grain is enclosed by oxygen-rich grain boundaries, which act as insulators and reduce the overall electrical conductivity. These grain boundaries play a crucial role in the electrical behavior at low frequencies. Alternatively, at higher frequencies, the conductive grains become dominant, driven by the localized hopping or polaron transport involving mixed Fe^{3+}/Fe^{4+} states. The marked increase in σ_{AC} for the ceramic sintered at 1200 °C (approximately 0.4 S/m at 1 MHz) can be attributed to significant grain growth, consistent with SEM observations (Figure 5). Analogous behavior was reported in Sm-doped ceramics, where a sample sintered at a higher temperature, yielding the highest grain size, achieved the highest conductivity among comparative samples [66]. General studies on oxide ceramics substantiate that grain size increases with sintering temperature, a key factor enhancing conductivity by reducing grain-boundary hindrance [67,68]. In addition, the electrical transport in $CaFeO_{3-\delta}$ is also governed by defect chemistry. In Fe-based perovskites, oxygen non-stoichiometry δ is thermodynamically dependent on temperature and oxygen partial pressure, and variations in δ are charge-compensated by changes in Fe valence (Fe^{3+}/Fe^{4+}). Therefore, changes in sintering temperature (and the associated oxygen exchange during sintering/cooling in air) can tune δ and the Fe^{3+}/Fe^{4+} balance, directly influencing small polaron/defect-assisted conduction pathways [49,50].

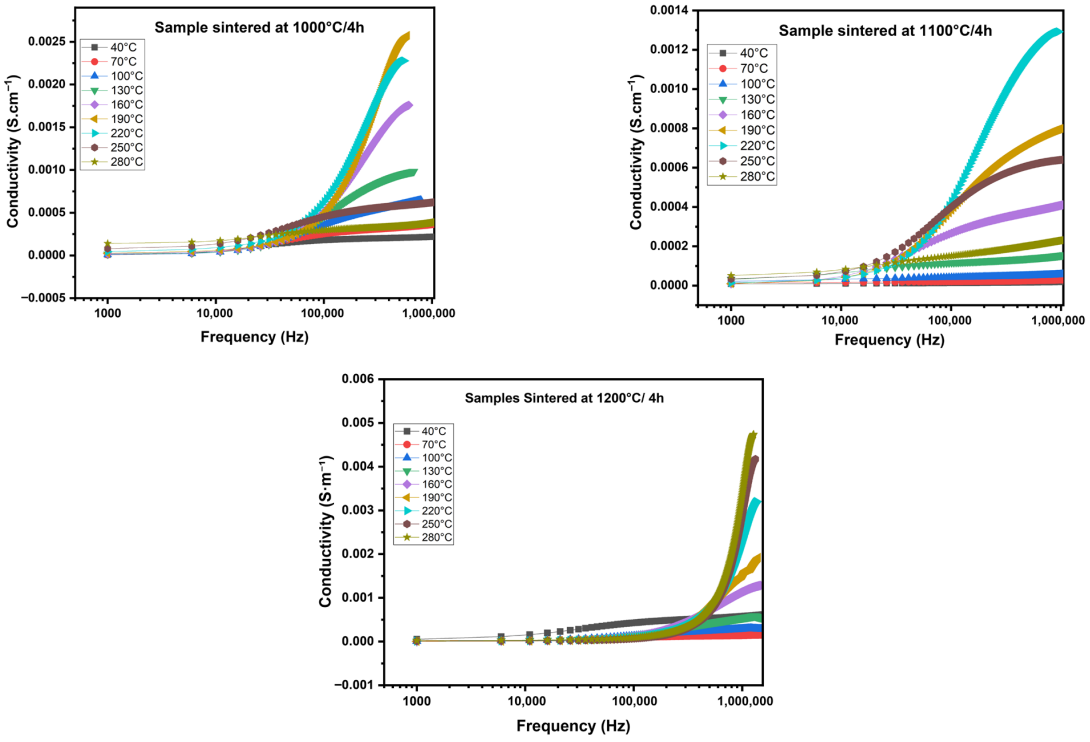

Figure 8. Conductivity (σ) as a function of frequency for all the $CaFeO_{3-\delta}$ ceramics sintered at different temperatures.

Moreover, Jonscher's law [61] describes the Universal Dynamic Response (UDR), where the AC conductivity depends on frequency [69], according to Equation (6):

$$\sigma = \sigma_{DC} + A\omega^s \quad (6)$$

s is the exponent value, indicating the interaction degree between mobile ions and the lattice. A is a temperature-dependent parameter that also influences this interaction. According to the data, the s values range from 0 to 1.

For all samples, s(T) exhibits a non-monotonic trend: It increases with temperature up to a maximum and then decreases at higher temperatures. As summarized in Table 4, T_{max} is 220 °C for the ceramics sintered at 1000 °C and 1100 °C, while it shifts to 280 °C for the 1200 °C sample. This behavior indicates a crossover between two localized transport regimes. In the low/intermediate-temperature region (from 40 °C up to T_{max}), where s increases with T, the conduction is consistent with tunneling-assisted localized transport (NSPT-like). Above T_{max}, where s decreases with further temperature increase, the behavior becomes compatible with a correlated barrier hopping (CBH-type) contribution, which can be enhanced by grain-boundary potential barriers in polycrystalline ceramics [70].

Table 4. Maximum frequency exponent (s_{max}) and corresponding temperature (T_{max}) derived from Jonscher analysis.

Samples	S_{max}	T_{max} °C	Observation
CFO sintered 1000 °C/4 h	0.775	220	s increases to 220 °C and then decreases
CFO sintered 1100 °C/4 h	0.593	220	s increases to 220 °C and then decreases
CFO sintered 1200 °C/4 h	0.883	280	s increases to 280 °C and then decreases

To determine the activation energy, E_a of $CaFeO_{3-\delta}$ ceramics at 1 kHz, the Arrhenius law (Equation (7)) was applied to the DC conductivity σDC extracted from the low-frequency plateau of the conductivity spectra (the value at 1 kHz lies within this plateau for all samples). The Arrhenius fit was performed only over the temperature interval where $\ln(\sigma_{DC})$ versus (1000/T) exhibits a clear linear behavior, corresponding to approximately 60–227 °C. The findings are presented in Figure 9, illustrating the evolution of $\ln(\sigma_{DC})$ as a function of (1000/T) [71].

$$\sigma = \sigma_0 e^{-E_a/kT} \quad (7)$$

where σ_0: the pre-exponential factor, k: the Boltzmann constant, T: temperature, and E_a the activation energy. The conductivity of the samples increases with an increase in temperature, confirming semiconductor behavior. In order to determine the activation energy for the samples, the logarithm of conductivity (σ_{DC}) as a function of the inverse of temperature 1000/T was plotted in Figure 9, and the results are summarized in Table 5. The activation energy of the samples found at 1 kHz varies from approximately 0.15 eV to 0.39 eV. This suggests that the internal defect formation in the present ceramics is mainly attributed to oxygen vacancies. The sample sintered at 1200 °C/4 h recorded the minimum activation energy, indicating that charge transport requires less thermal energy. This behavior can be attributed to structural improvements at higher sintering temperatures, such as enhanced crystallinity, as confirmed by XRD analysis, and optimized grain boundaries along with increased grain size and density. These microstructural changes facilitate faster conduction, which may explain its higher conductivity compared to the other samples. The sample sintered at 1200 °C demonstrates the lowest E_a and highest conductivity, while the 1100 °C sample shows the highest E_a and lowest conductivity. This trend is microstructurally driven: Sintering at 1200 °C coarsens grains and refines grain boundaries, reducing the interfacial barrier height and the energy cost for carrier hopping. This facilitates more

delocalized transport, yielding higher conductivity. Conversely, the finer grains and abundant resistive boundaries in the 1100 °C ceramic enhance carrier localization, resulting in a higher E_a and lower conductivity. Similar trends have been reported in lithium–zinc ferrites, where conductivity increased and activation energy decreased with rising sintering temperature [72]; in gadolinium-doped ceria, where increased grain size and density (shown by XRD/SEM) corresponded with improved conductivity and lower activation energy [73]; and in BiCuSeO systems, where larger crystallite size correlated with enhanced electrical transport [74].

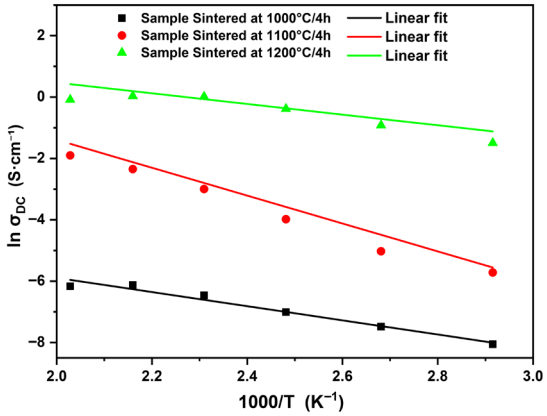

Figure 9. ln(σ_{DC}) as a function of the inverse of temperature (1000/T) for all the ceramics sintered at different temperatures.

Table 5. Activation energy at 1 kHz.

Samples Sintered at:	E_a (ev)
1000 °C/4 h	0.199 ev
1100 °C/4 h	0.392 ev
1200 °C/4 h	0.150 ev

It is worth mentioning that the complex impedance spectroscopy method can be used to study the electrical relaxation behavior of materials and to separate the effects of grain and grain boundaries in electroceramics. To achieve this, the Cole–Cole plot is used to investigate the complex impedance. Figure 10a displays the adjusted plots of the sample sintered at 1100 °C/4 h based on two parallel combinations: (R1, C1) and (R2, CPE1), connected in series, illustrating the contribution of the ceramic grains at high frequencies and the grain boundaries at low frequencies. From the fitting analysis, the resistance R1 and R2, corresponding to the grain resistance (RG) and grain-boundary resistance (RGB), were determined. It is important to note that the behavior of all the other samples is similar. In the tested samples, two semi-arcs were observed: The first is attributed to the contribution of the grains, while the other is attributed to the contribution of the grain boundaries. As the temperature increases, the radius of the semicircles decreases, thus indicating a Negative Thermal Resistivity Coefficient (NTCR) behavior in the material [75]. This radius variation is a typical feature of semiconductors, which indicates a non-ideal Debye relaxation behavior [76]. This could be attributed to several causes, including deformation, stress phenomena, atomic defect distribution, and grain and grain boundary orientation. Additionally, it was observed that, when the temperature increases, the semicircles are gradually reduced. In line with the IBLC model, these phenomena are generally associated with the existence of a distribution of relaxation times, where the resulting complex impedance is represented by two overlapping semicircles [77]. Figure 10b presents the

Nyquist plots of all samples sintered at various temperatures, measured at 220 °C. From the fitting procedure, the resistances RG and RGB were extracted. Similar impedance behavior was observed for all samples. As shown in Table 6, the grain-boundary resistance is significantly higher than the grain resistance (RGB > RG) for all sintering temperatures. Similar impedance trends were observed at other temperatures of measurement, with grain-boundary resistance consistently higher than grain resistance (RGB > RG) for all sintering conditions, indicating that grain boundaries dominate the resistive response, in agreement with the internal barrier layer capacitor (IBLC) mode. In addition, the reduction in the semicircle radius with increasing temperature reflects the typical negative temperature coefficient of resistance (NTCR) behavior characteristic of semiconducting oxides [78]. This behavior can also be related to the increase in grain size with sintering temperature, as observed in the SEM micrographs (Figure 5). Larger grains reduce the number of grain boundaries per unit volume, which decreases the overall grain-boundary contribution to the electrical resistance and enhances the conductivity of the ceramics. This behavior is consistent with impedance studies on semiconducting perovskite oxides, where the total resistance is often dominated by the grain-boundary contribution (RGB > RG). For instance, Alzahrani et al. reported that Nyquist fitting in a semiconducting perovskite yields RGB larger than RG, confirming grain-boundary-controlled transport, and they further related the sintering-temperature dependence of the impedance response to microstructural evolution [79]. Similarly, in semiconducting ZnO-based ceramics, the sintering temperature was shown to strongly affect grain-boundary barrier properties and grain-boundary resistance, through microstructural development and defect redistribution at grain boundaries [80].

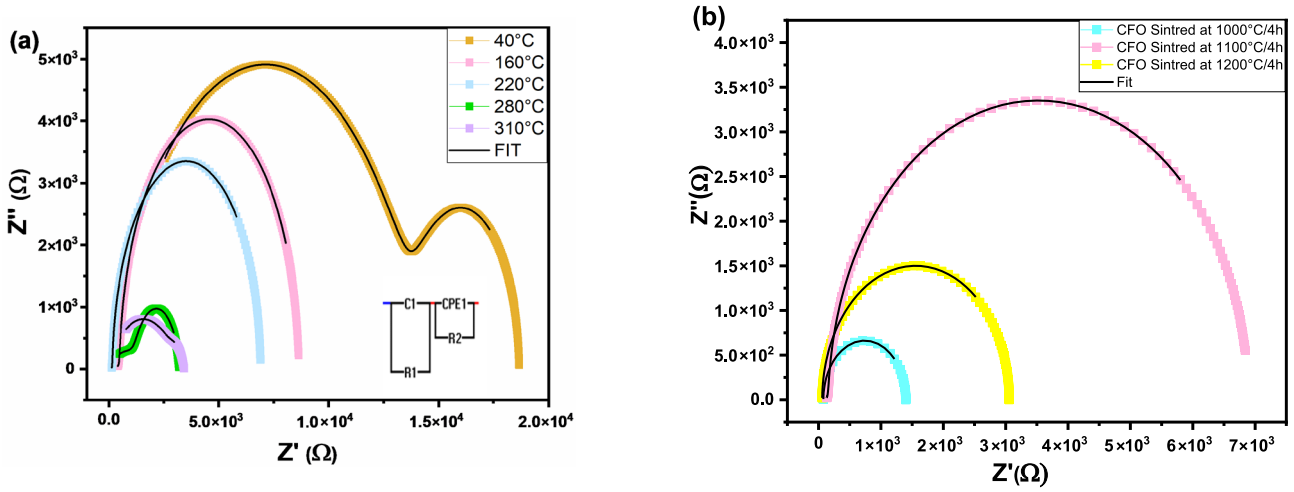

Figure 10. (**a**): Nyquist plots of the impedances of $CaFeO_{3-\delta}$ sintered at 1100 °C/4 h. (**b**): Nyquist plots at 220 °C of all the samples sintered at different temperatures.

Table 6. Grain and grain-boundary resistances for the $CaFeO_{3-\delta}$ ceramics at 220 °C.

Samples Sintered at:	R_G (Ω)	R_{GB} (Ω)
1000 °C/4 h	77.3	1491.2
1100 °C/4 h	135.7	8172.9
1200 °C/4 h	58.4	2998.2

3.6. Gas Sensing Properties

(A) Experiment

To assess the potential of $CaFeO_{3-\delta}$ samples sintered at different temperatures for gas sensing applications, qualitative electrical measurements were conducted in ethanol

vapors. The detection properties were tested by cycling the ceramics in both an open-air atmosphere and an ethanol/air medium to evaluate the sensitivity and reproducibility. The response is calculated by Formula (8):

$$R\% = \frac{R(air) - R(ethanol)}{R(air)} \times 100 \quad (8)$$

The ethanol-sensing performance of the $CaFeO_{3-\delta}$ ceramics was assessed through impedance spectroscopy by alternately exposing the samples to ambient air and ethanol vapors. During the testing, the real part of the impedance (R) was continuously monitored, and the sensor response was calculated as its percentage change when the atmosphere was switched from pure air to ethanol vapor. This parameter reflects how efficiently the material detects ethanol, relative to its baseline electrical behavior in air [81]. Figure 11a–c shows the results of four consecutive exposure–recovery cycles for each sintering temperature. For each cycle, the sample was exposed to ethanol vapors for 120 s, followed by 120 s in air. The 120 s exposure time was selected after preliminary trials demonstrating that the impedance reached a steady value within this period, ensuring reproducible measurements.

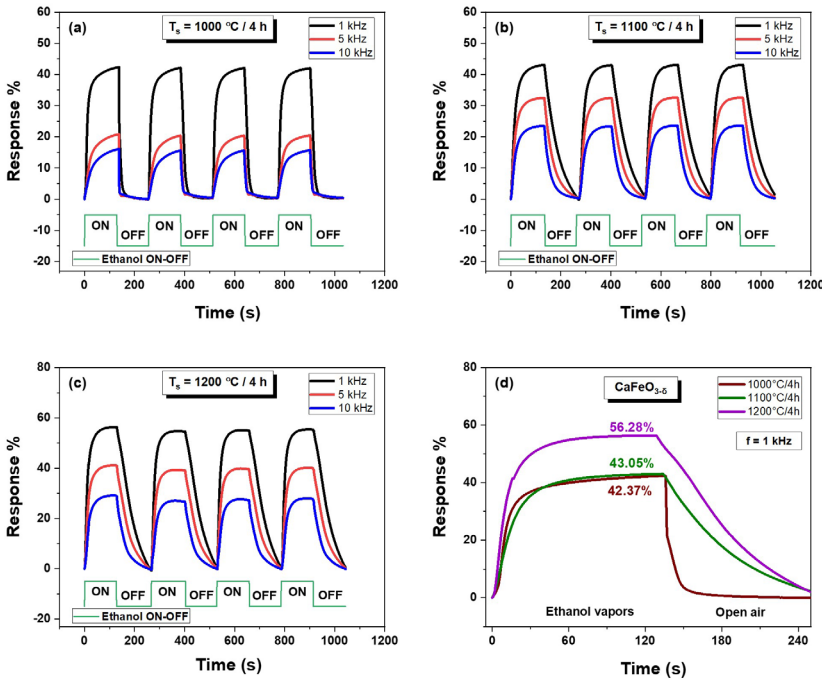

Figure 11. (**a**–**c**) Gas sensitivity responses of $CaFeO_{3-\delta}$ ceramics sintered at different temperatures (ethanol/air atmosphere at room temperature for 4 cycles) and (**d**) comparison of the impedance response of all samples during one exposure cycle.

Upon exposure to ethanol vapor, all the samples showed a clear decrease in impedance, indicating the adsorption of ethanol molecules onto the $CaFeO_{3-\delta}$ surface and the consequent release of electrons back to the near-surface region. Such an electron-dominated (n-type) response is consistent with thermoelectric reports on $CaFeO_{3-\delta}$, where a negative Seebeck coefficient indicates that electrons are the majority charge carriers, supporting the n-type-like behavior observed here at room temperature [32]. This decreases the material's resistance, which is a typical behavior for n-type semiconducting perovskite oxides in the presence of a reducing gas [80,81]. When returned to the air, ethanol desorbs from the surface, and the impedance gradually recovers toward its initial value. The repetition of this reversible behavior over multiple cycles without significant drift confirms the stability, repeatability, and robustness of the sensor response, which are essential criteria for practical

gas sensor applications. Interestingly, among the studied samples, the pellets sintered at 1200 °C exhibited the highest ethanol response (56.28%) (Figure 11d). This is particularly noteworthy because this sample has a relatively dense microstructure (~90% relative density) and a larger average grain size (≈2.32 μm). Usually, porous structures with smaller grains are preferred in gas sensing, because a higher surface area favors the adsorption of gas molecules [82]. However, in the case of $CaFeO_{3-\delta}$, the sensing mechanism not only depends on surface adsorption but is also strongly governed by the efficiency of charge transport within the sensing layer [83]. The high-density microstructure of the 1200 °C sample provides better grain-to-grain contact, reduces the number of grain boundaries (which act as charge trapping sites), and decreases the internal electrical resistance. As a result, the electrons released upon ethanol adsorption are more effectively transported throughout the material, producing a larger and more uniform change in conductivity.

In contrast, the samples sintered at 1000 °C and 1100 °C possess higher porosity and smaller grains, which theoretically provide more active surface for adsorption. However, their internal conduction pathways are less well-connected, with a higher density of grain boundaries acting as scattering centers for the charge carriers. These structural shortcomings interrupt or delay the propagation of the resistance change through the sample, which explains their comparatively lower responses (42.37% and 43.00%, respectively). In mixed ionic–electronic conductors like $CaFeO_{3-\delta}$, the chemiresistive signal reflects two coupled steps: surface redox of ethanol with adsorbed oxygen species, and vacancy-assisted bulk transport/re-oxidation of the Fe–O network. Such vacancy-assisted transport and surface oxygen exchange are widely reported to be enhanced by oxygen-vacancy populations and mixed Fe valence states; moreover, oxygen non-stoichiometry δ in Fe-based perovskites is thermodynamically dependent on temperature and oxygen partial pressure, so the sintering or cooling history provides a rational route to influence δ and the Fe^{3+}/Fe^{4+} balance, and consequently the conductivity modulation driven by oxygen adsorption/desorption during sensing, consistent with the sensing mechanism literature and defect-chemistry reports, as reported by Souri et al., and Vuong et al. [50,78]. In dense ceramics, continuous grain–grain contacts reduce grain-boundary barriers and contact constrictions, so carrier/defect modulations created at the surface are transmitted more efficiently through the bulk path. Conversely, in porous bodies, many GB barriers and narrow necks screen a fraction of the surface reaction and raise the baseline resistance, which limits the net response. The oxygen-vacancy population (δ) further amplifies the effect by increasing active adsorption/exchange sites and accelerating surface-exchange/bulk diffusion. Impedance fitting performed over the entire investigated temperature range shows that the grain-boundary resistance remains higher than the grain (bulk) resistance (RGB > RG) for all samples, indicating that grain boundaries constitute the dominant resistive element in the electrical response [82–85]. In addition, the lowest-C sample (1200 °C) found in the EDX results shows the highest ethanol response (56.28%), consistent with cleaner, better-connected surfaces/grain paths. This reveals that, for $CaFeO_{3-\delta}$ ceramics, an optimal balance between surface reactivity and charge transport is critical, and that densification can outweigh surface area effects in determining gas sensitivity [86].

Additionally, the enhanced performance of the 1200 °C sample can be related to defect-mediated surface reactivity and oxygen-vacancy-related active sites, which are known to depend on thermal history and oxygen activity in ferrite perovskites. Oxygen vacancies play a key role as active adsorption sites for ethanol, facilitating rapid interaction between the gas molecules and the sensor surface. Although relatively few studies have explored ethanol sensing in $CaFeO_{3-\delta}$, the high response observed in this work indicates strong potential for this material as a sensitive, low-cost ethanol sensor operating at room temperature. In addition to high sensitivity, the $CaFeO_{3-\delta}$ sensor also demonstrates fast dynamic response,

an essential attribute for real-time gas detection. The response time ($t_{90}\uparrow$) is defined as the time elapsed between the introduction of ethanol and the moment when the impedance reaches 90% of its total change relative to the baseline in air. The recovery time ($t_{90}\downarrow$) is defined as the time required, after switching back to air, for the impedance to return 90% of the way toward its baseline value. The measured $t_{90}\uparrow$ values are narrowly distributed (30–31 s) for all pellets, indicating a similar initial adsorption/interaction kinetics with ethanol. In contrast, $t_{90}\downarrow$ varies significantly (17–120 s), which increases systematically with the sintering temperature. This trend reflects microstructural effects: The pellet sintered at 1200 °C, being denser and composed of larger, better-connected grains, requires a slower vacancy-assisted bulk re-oxidation once ethanol desorbs. The pellets sintered at 1000–1100 °C are more porous and dominated by shallow surface and grain-boundary depletion layers, which re-oxidize rapidly, leading to faster recovery times. Full recovery of the baseline signal after multiple cycles further confirms the reversibility of ethanol adsorption and desorption processes and attests to the excellent operational stability of the sensor. To highlight the importance of this finding, the obtained response (56.28%) at room temperature is higher than that reported for many other perovskite-based sensors operating at substantially higher temperatures. For example, $Bi_{0.95}Sr_{0.05}FeO_3$ shows ~49.5% response at 208 °C to 200 ppm ethanol [16], while $La_{0.9}Fe_{0.85}Co_{0.15}O_3$ achieves ~50.45% at 200 °C for 100 ppm ethanol [86]. In contrast, our $CaFeO_{3-\delta}$ sensor achieves superior performance at room temperature, which eliminates the need for heating elements and significantly reduces energy consumption, making it better suited for practical applications.

(B) Gas sensing mechanism

Figure 12 presents the proposed gas sensing mechanism. In an open-air environment, the molecule of oxygen adsorbs onto the surface of the detecting samples of $CaFeO_{3-\delta}$ [10], forming ions of oxygen such as O_2^-, O_2^{2-}, or O^- by the capture of free electrons from the conduction band, because oxygen molecules interact as electron acceptors, as illustrated by Equations (9)–(12). The decrease in the electron concentration increases the sensor resistance.

$$O_{2(gas)} \leftrightarrow O_{2(ads)} \tag{9}$$

$$O_{2(ads)} + e^- \leftrightarrow O^-_{2(ads)} \tag{10}$$

$$O^-_{2(ads)} + e^- \leftrightarrow 2\,O^-_{2(ads)} \tag{11}$$

$$O^-_{(ads)} + e^- \leftrightarrow O^{2-}_{(ads)} \tag{12}$$

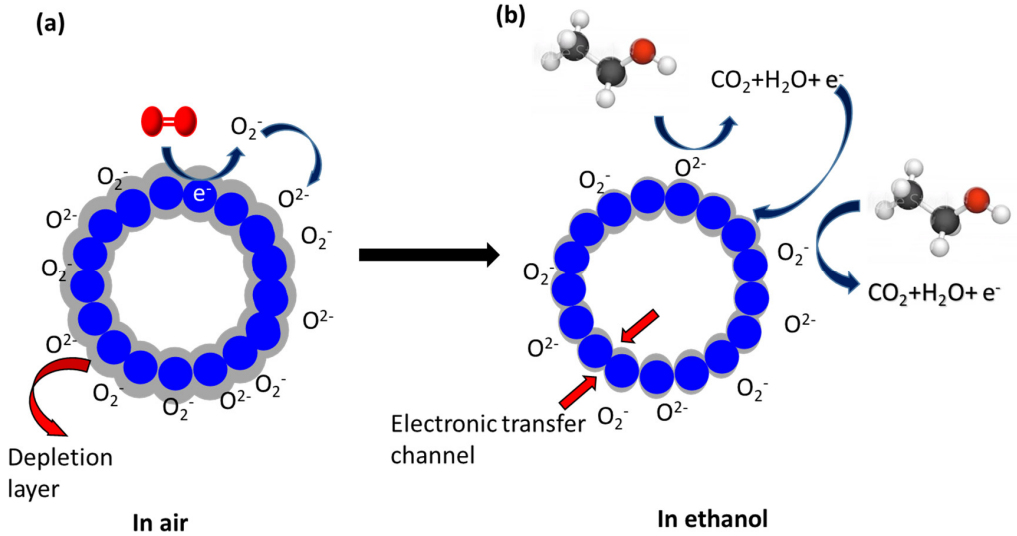

Figure 12. Schematic of the reaction on the ceramic semiconductor surface, (**a**) in air and (**b**) in ethanol.

When ethanol is present, the gas molecules act with the O_2^{2-}, or O^-, releasing the trapped electrons back into the conduction band. This release decreases the material's resistance, and the extent of the resistance change correlates directly with the gas concentration being measured, as described by Equations (13) and (14) [10]. After removing the ethanol gas from the system, the resistance quickly returned to its original value, ensuring excellent long-term stability of the $CaFeO_{3-\delta}$ gas sensors when purged with air [8].

$$C_2H_5OH_{(gas)} + 6\,O^-_{(ads)} \leftrightarrow 2\,CO_2 + 3H_2O + 6e^- \quad (13)$$

$$C_2H_5OH_{(gas)} + 6\,O^{2-}_{(ads)} \leftrightarrow 2\,CO_2 + 3H_2O + 12e^- \quad (14)$$

4. Conclusions

$CaFeO_{3-\delta}$ ceramic samples were produced using a solid-state reaction to investigate whether their dielectric and conductive properties are affected by sintering temperature. XRD analyses show that all the ceramics belong to the Pcmn space group in a pure orthorhombic phase. The crystallographic data indicate no regular change in unit cell parameters or volume as the sintering temperature increases. Higher sintering temperatures lead to improved crystallinity, larger crystallites, and increased grain size due to enhanced grain growth. The dielectric constant of $CaFeO_{3-\delta}$ ceramics decreases with increasing frequency until it levels off at high frequencies, with a colossal permittivity value ($\varepsilon' = 2.1 \times 10^5$) observed in the sample sintered at 1200 °C for 4 h. The highest AC conductivity was also recorded for this sample, which is likely owing to the larger grain size. Cole–Cole analysis confirmed deviations from Debye's ideal behavior. Moreover, dielectric relaxation relates to the strong correlation between iron conduction and dielectric properties. The sample sintered at 1200 °C for 4 h exhibits enhanced electrical conduction at high frequencies and high permittivity at low frequencies, making it an excellent candidate for batteries and electronic capacitors. Preliminary qualitative tests conducted under saturated ethanol vapors assessed gas detection capabilities at room temperature and normal pressure. The ferrite samples showed consistent results across multiple tests, with the highest sensitivity in the sample sintered at 1200 °C for 4 h, attributable to its weakened electrical conductivity at low frequencies. Notably, the relaxation time of the $CaFeO_{3-\delta}$ sample sintered at 1000 °C for 4 h is shorter than that of other samples. In summary, $CaFeO_{3-\delta}$ ceramics with a perovskite structure display promising electrical properties and are suitable for various technological applications, including capacitors, signal transmission, gas sensors, and other electronic components.

Author Contributions: Conceptualization, A.B., N.G., F.Z.A. and T.-d.L.; Methodology, A.B. and N.G.; Software, A.B., I.T., L.-E.U. and F.A.; Validation, A.B., L.M., F.Z.A. and T.-d.L.; Formal analysis, A.B., I.T. and F.A.; Investigation, N.G., Ina Turcan, F.G., L.-E.U., L.L., L.M., F.Z.A. and T.-d.L.; Data curation, A.B., I.T., F.G., L.-E.U., L.L. and F.A.; Writing—original draft, A.B.; Writing—review & editing, A.B., N.G., F.G., L.L., L.M., F.Z.A. and T.-d.L.; Visualization, F.G., L.M., F.Z.A., T.-d.L. and F.A.; Supervision, L.L., L.M. and T.-d.L. All authors have read and agreed to the published version of the manuscript.

Funding: This research received no external funding.

Data Availability Statement: The data that support the findings of this study are available from the corresponding authors upon reasonable request.

Conflicts of Interest: The authors declare no conflicts of interest.

References

1. Panda, S.; Mehlawat, S.; Dhariwal, N.; Sanger, A.; Kumar, A. Comprehensive review on gas sensors: Unveiling recent developments and addressing challenges. *Mater. Sci. Eng. B* **2024**, *308*, 117616. [CrossRef]
2. Saruhan, B.; Lontio Fomekong, R.; Nahirniak, S. Review: Influences of Semiconductor Metal Oxide Properties on Gas Sensing Characteristics. *Front. Sens.* **2021**, *2*, 657931. [CrossRef]
3. Bagwaiya, T.; Bhattacharya, S.; Shelke, V.; Samanta, S.; Kaur, M.; Debnath, A.K. Enhanced H_2S gas sensing performance of Ca-doped Bismuth Ferrite thick films. *Mater. Sci. Semicond. Process.* **2022**, *148*, 106782. [CrossRef]
4. Mukherjee, C.; Mondal, D.; Sarkar, M.; Das, J. Nanocrystalline Nickel Zinc Ferrite as an efficient alcohol sensor at room temperature. *Int. J. Environ. Agric. Biotechnol.* **2017**, *2*, 799–804. [CrossRef]
5. Fidelus, J.D.; Łojkowski, W.; Millers, D.; Smits, K.; Grigorjeva, L. Advanced nanocrystalline ZrO_2 for optical oxygen sensors. In *SENSORS, 2009 IEEE*; IEEE: Piscataway, NJ, USA, 2009; pp. 1268–1272. [CrossRef]
6. Klym, H.; Ingram, A.; Hadzaman, I.; Karbovnyk, I.; Vasylchyshyn, I.; Popov, A.I. Nanoporous characterization of modified humidity-sensitive MgO-Al_2O_3 ceramics by positron annihilation lifetime spectroscopy method. *IOP Conf. Ser. Mater. Sci. Eng.* **2019**, *503*, 012019. [CrossRef]
7. Rathore, D.; Kurchania, R.; Pandey, R.K. Nanoferrites gas sensors: A critical review. *Sens. Actuators A Phys.* **2024**, *379*, 115968. [CrossRef]
8. Tong, T.; Chen, J.; Jin, D.; Cheng, J. Preparation and gas sensing characteristics of $BiFeO_3$ crystallites. *Mater. Lett.* **2017**, *197*, 160–162. [CrossRef]
9. Murugesan, C.; Chandrasekaran, G. Enhanced Electrical and Magnetic Properties of Annealed Magnesium Ferrite Nanoparticles. *J. Supercond. Nov. Magn.* **2015**, *28*, 3607–3615. [CrossRef]
10. Zhou, X.; Liu, J.; Wang, C.; Sun, P.; Hu, X.; Li, X.; Shimanoe, K.; Yamazoe, N.; Lu, G. Highly sensitive acetone gas sensor based on porous $ZnFe_2O_4$ nanospheres. *Sens. Actuators B Chem.* **2015**, *206*, 577–583. [CrossRef]
11. Yu, Q.; Zhang, Y.; Xu, Y. Hierarchical hollow $BiFeO_3$ microcubes with enhanced acetone gas sensing performance. *Dalton Trans.* **2021**, *50*, 6702–6709. [CrossRef]
12. Njoroge, M.A.; Kirimi, N.M.; Kuria, K.P. Spinel ferrites gas sensors: A review of sensing parameters, mechanism and the effects of ion substitution. *Crit. Rev. Solid State Mater. Sci.* **2022**, *47*, 807–836. [CrossRef]
13. Koli, P.B.; Kapadnis, K.H.; Deshpande, U.G. Nanocrystalline-modified nickel ferrite films: An effective sensor for industrial and environmental gas pollutant detection. *J. Nanostruct. Chem.* **2019**, *9*, 95–110. [CrossRef]
14. Dong, G.; Fan, H.; Tian, H.; Fang, J.; Li, Q. Gas-sensing and electrical properties of perovskite structure p-type barium-substituted bismuth ferrite. *RSC Adv.* **2015**, *5*, 29618–29623. [CrossRef]
15. Korotcenkov, G. Metal oxides for solid-state gas sensors: What determines our choice? *Mater. Sci. Eng. B* **2007**, *139*, 1–23. [CrossRef]
16. Xu, H.; Xu, J.; Li, H.; Zhang, W.; Zhang, Y.; Zhai, Z. Highly sensitive ethanol and acetone gas sensors with reduced working temperature based on Sr-doped $BiFeO_3$ nanomaterial. *J. Mater. Res. Technol.* **2022**, *17*, 1955–1963. [CrossRef]
17. Li, F.; Wang, S.; Wu, Z.; Xiong, X.; Li, J.; Zhou, J.; Gao, X. Excellent ethanol sensor based on $LaFeO_3$ modified with gold nanoparticles. *J. Mater. Sci. Mater. Electron.* **2021**, *32*, 27587–27595. [CrossRef]
18. Yu, J.; Wang, C.; Yuan, Q.; Yu, X.; Wang, D.; Chen, Y. Ag-Modified Porous Perovskite-Type $LaFeO_3$ for Efficient Ethanol Detection. *Nanomaterials* **2022**, *12*, 1768. [CrossRef] [PubMed]
19. Abdel-Khalek, E.K.; Motawea, M.A.; Aboelnasr, M.A.; El-Bahnasawy, H.H. Study the oxygen vacancies and Fe oxidation states in CaFeO3-δ perovskite nanomaterial. *Phys. B Condens. Matter* **2022**, *624*, 413415. [CrossRef]
20. Benatia, A.; Gouitaa, N.; Lamcharfi, T.-d.; Abdi, F.; Haddad, M. Effect of calcination temperature and duration on structural and dielectric properties of $CaFeO_3$-δ. *Arab. J. Chem.* **2024**, *17*, 105407. [CrossRef]
21. Zhang, H.; Shi, H.; You, H.; Su, M.; Huang, L.; Zhou, Z.; Zhang, C.; Zuo, J.; Yan, J.; Xiao, T.; et al. Cu-doped $CaFeO_3$ perovskite oxide as oxygen reduction catalyst in air cathode microbial fuel cells. *Environ. Res.* **2022**, *214*, 113968. [CrossRef]
22. Woodward, P.; Cox, D.; Moshopoulou, E. Structural studies of charge disproportionation and magnetic order. *Phys. Rev. B Condens. Matter Mater. Phys.* **2000**, *62*, 844–855. [CrossRef]
23. Rogge, P.C.; Chandrasena, R.U.; Cammarata, A.; Green, R.J.; Shafer, P.; Lefler, B.M.; Huon, A.; Arab, A.; Arenholz, E.; Lee, H.N.; et al. Electronic structure of negative charge transfer $CaFeO_3$ across the metal-insulator transition. *Phys. Rev. Mater.* **2018**, *2*, 015002. [CrossRef]
24. Ghosh, B.; Mahato, D.K.; Banerjee, S. Formation of Magnetic Glass by Kinetic Arrest of First Order Magnetic Phase Transition in $CaFeO_3$. *Mater. Today Proc.* **2018**, *5*, 15426–15430. [CrossRef]
25. Morimoto, S.; Yamanaka, T.; Tanaka, M. Structure and electron density distribution of $CaFeO_3$ in the "charge disproportionate" state. *Phys. B Condens. Matter* **1997**, *237–238*, 66–67. [CrossRef]
26. Huang, T.; Wang, Y.; Li, H.; Wang, M.; Lyu, Y.; Shen, S.; Lu, N.; He, Q.; Yu, P. Tuning the electronic properties of epitaxial strained $CaFeO_3$-δ thin films. *Appl. Phys. Lett.* **2019**, *114*, 221907. [CrossRef]

27. Shin, Y.; Doh, K.Y.; Kim, S.H.; Lee, J.H.; Bae, H.; Song, S.J.; Lee, D. Effect of oxygen vacancies on electrical conductivity of $_{La0.5}Sr_{0.5}FeO_3-\delta$ from first-principles calculations. *J. Mater. Chem. A* **2020**, *8*, 4784–4789. [CrossRef]
28. Pokhriyal, P.; Bhakar, A.; Sinha, A.K.; Sagdeo, A. Colossal dielectric permittivity and mechanism of AC conduction in bulk delafossite $CuFeO_2$. *J. Appl. Phys.* **2019**, *125*, 164101. [CrossRef]
29. Mao, P.; Wang, J.; Liu, S.; Zhang, L.; Zhao, Y.; He, L. Grain size effect on the dielectric and non-ohmic properties of $CaCu_3Ti_4O_{12}$ ceramics prepared by the sol-gel process. *J. Alloys Compd.* **2019**, *778*, 625–632. [CrossRef]
30. Slaoui, M.; Gouitaa, N.; Harrach, A.; Abdi, F.; Lamcharfi, T. Effect of $Pb_{0.8}La_{0.2}Ti_{0.95}O_3$ Doping on the Electrical and Dielectric Properties of CCTO Compound Synthesized by Hybrid Method. *Mater. Sci. Forum* **2023**, *1096*, 49–70. [CrossRef]
31. Dai, Y.; Li, H.; Wang, Y.; Zhong, K.; Zhang, H.; Yu, J.; Huang, Z.; Yan, J.; Huang, L.; Liu, X.; et al. Zn-doped $CaFeO_3$ perovskite-derived high performed catalyst on oxygen reduction reaction in microbial fuel cells. *J. Power Sources* **2021**, *489*, 229498. [CrossRef]
32. Khan, M.N.; Zafar, N. Structural, Electric and Thermoelectric Studies of $CaFeO_3$ System. *Nucleus* **2015**, *52*, 25–28. [CrossRef]
33. Himabindu, B.; Latha Devi, N.S.M.P.; Rajini Kanth, B. Microstructural parameters from X-ray peak profile analysis by Williamson-Hall models; A review. *Mater. Today Proc.* **2021**, *47*, 4891–4896. [CrossRef]
34. Nath, D.; Singh, F.; Das, R. X-ray diffraction analysis by Williamson-Hall, Halder-Wagner and size-strain plot methods of CdSe nanoparticle—A comparative study. *Mater. Chem. Phys.* **2020**, *239*, 122021. [CrossRef]
35. Mesrar, M.; Lamcharfi, T.; Echatoui, N.S.; Abdi, F. Effect of sintering temperature on the microstructure and electrical properties of $(Na_{0.5}Bi_{0.5})TiO_3$ processed by the sol-gel method. *J. Sol-Gel Sci. Technol.* **2022**, *103*, 820–831. [CrossRef]
36. Li, J.; Kou, X.; Qin, Y.; He, H. Microstructure and magnetic properties of $La_{1-x}Sr_xFeO_3$ nanoparticles. *Phys. Status Solidi Appl. Res.* **2002**, *191*, 255–259. [CrossRef]
37. Lin, Q.; Yang, X.; Lin, J.; Guo, Z.; He, Y. The structure and magnetic properties of magnesium-substituted $LaFeO_3$ perovskite negative electrode material by citrate sol-gel. *Int. J. Hydrogen Energy* **2018**, *43*, 12720–12729. [CrossRef]
38. Lebid, M.; Omari, M. Synthesis and Electrochemical Properties of $LaFeO_3$ Oxides Prepared via Sol-Gel Method. *Arab. J. Sci. Eng.* **2014**, *39*, 147–152. [CrossRef]
39. Kucharczyk, B.; Okal, J.; Tylus, W.; Winiarski, J.; Szczygieł, B. The effect of the calcination temperature of $LaFeO_3$ precursors on the properties and catalytic activity of perovskite in methane oxidation. *Ceram. Int.* **2019**, *45*, 2779–2788. [CrossRef]
40. Deka, S.; Saxena, V.; Hasan, A.; Chandra, P.; Pandey, L.M. Synthesis, characterization and in vitro analysis of α-Fe_2O_3-$GdFeO_3$ biphasic materials as therapeutic agent for magnetic hyperthermia applications. *Mater. Sci. Eng. C* **2018**, *92*, 932–941. [CrossRef]
41. Ghosh, S.; Kamaraju, N.; Seto, M.; Fujimori, A.; Takeda, Y.; Ishiwata, S.; Kawasaki, S.; Azuma, M.; Takano, M.; Sood, A.K. Raman scattering in $CaFeO_3$ and $La_{0.33}Sr_{0.67}FeO_3$ across the charge-disproportionation phase transition. *Phys. Rev. B Condens. Matter Mater. Phys.* **2005**, *71*, 245110. [CrossRef]
42. Weber, M.C.; Guennou, M.; Zhao, H.J.; Íñiguez, J.; Vilarinho, R.; Almeida, A.; Moreira, J.A.; Kreisel, J. Raman spectroscopy of rare-earth orthoferrites $RFeO_3$ (R = La, Sm, Eu, Gd, Tb, Dy). *Phys. Rev. B* **2016**, *94*, 214103. [CrossRef]
43. Islam, M.A.; Xie, Y.; Scafetta, M.D.; May, S.J.; Spanier, J.E. Raman scattering in $La_{1-x}Sr_xFeO_{3-\delta}$ thin films: Annealing-induced reduction and phase transformation. *J. Phys. Condens. Matter* **2015**, *27*, 155401. [CrossRef]
44. Kozakov, A.T.; Kochur, A.G.; Torgashev, V.I.; Googlev, K.A.; Kubrin, S.P.; Trotsenko, V.G.; Bush, A.A.; Nikolskii, A.V. $Bi_{1-x}Ca_xFeO_{3-\delta}$ ($0 \leq x \leq 1$) ceramics: Crystal structure, phase and elemental composition, and chemical bonding from X-ray diffraction, Raman scattering, Mössbauer, and X-ray photoelectron spectra. *J. Alloys Compd.* **2016**, *664*, 392–405. [CrossRef]
45. Saini, B.C.; Jain, N.; Rao, D.K.; Singhal, V.; Verma, A.; Goudar, D.M.; Raju, K.; Pinto, D.G. Effect of Sintering Temperature on the Physical and Mechanical Characteristics of Fabricated ZrO_2–Cr–Ni–Ce–Y Composite. *J. Compos. Sci.* **2024**, *8*, 446. [CrossRef]
46. Khomchenko, V.A.; Kiselev, D.A.; Vieira, J.M.; Jian, L.; Kholkin, A.L.; Lopes, A.M.L.; Pogorelov, Y.G.; Araujo, J.P.; Maglione, M. Effect of diamagnetic Ca, Sr, Pb, and Ba substitution on the crystal structure and multiferroic properties of the $BiFeO_3$ perovskite. *J. Appl. Phys.* **2008**, *103*, 024105. [CrossRef]
47. Opitz, A.K.; Nenning, A.; Rameshan, C.; Kubicek, M.; Götsch, T.; Blume, R.; Hävecker, M.; Knop-Gericke, A.; Rupprechter, G.; Klötzer, B.; et al. Surface Chemistry of Perovskite-Type Electrodes During High Temperature CO_2 Electrolysis Investigated by Operando Photoelectron Spectroscopy. *ACS Appl. Mater. Interfaces* **2017**, *9*, 35847–35860. [CrossRef]
48. Oyane, A.; Sakamaki, I.; Koga, K.; Nakamura, M. Formation of a calcium phosphate layer with immobilized cobalt chromite nanoparticles on cobalt-chromium alloy by a laser-assisted biomimetic process. *Appl. Sci.* **2020**, *10*, 5584. [CrossRef]
49. Lohne, Ø.F.; Phung, T.N.; Grande, T.; Bouwmeester, H.J.M.; Hendriksen, P.V.; Søgaard, M.; Wiik, K. Oxygen Non-Stoichiometry and Electrical Conductivity of $La_{0.2}Sr_{0.8}Fe_{0.8}B_{0.2}O_{3-\delta}$, B = Fe, Ti, Ta. *J. Electrochem. Soc.* **2013**, *161*, F176. [CrossRef]
50. Vuong, J.; Derakhshan, S.; Tavassol, H. How Oxygen Deficiency and Its Ordering Control Electrical Conductivity in $Sr_{2-x}Ca_xFe_2O_{6-\delta}$ Perovskites as Related to Water Oxidation Electrocatalysis. *ACS Mater. Au* **2024**, *4*, 654–663. [CrossRef]
51. Tio, S.; Ramana, V.; Feng, L.; Lin, W.; Murty, B.S. Effect of grain size on dielectric and ferroelectric properties of nanostructured $Ba_{0.8}Sr_{0.2}TiO_3$ ceramics. *J. Adv. Ceram.* **2015**, *4*, 46–53. [CrossRef]
52. Najwa, G.; Zahra, A.F.; Taj-Dine, L.; Farid, A.; Mustapha, H. High Dielectric Permittivity and Low Transition Temperature of $(1 - x)CaTiO_{3-x}FeTiO_3$ Inorganic Composites (x = 0.0 to 1.0). *Russ. J. Inorg. Chem.* **2022**, *67*, 1868–1879. [CrossRef]

53. Slaoui, M.; Najwa, G.; Issmaeli, Y.E.; Abdi, F. Effect of Zinc Doping on the Electrical and Dielectric Properties of CCTO Compound Synthesized by Solid-State Method. *Asian J. Chem.* **2021**, *33*, 2000–2006. [CrossRef]
54. Jonscher, A.K. Dielectric relaxation in solids. *J. Phys. D. Appl. Phys.* **1999**, *32*, R57. [CrossRef]
55. Patankar, K.K.; Dombale, P.D.; Mathe, V.L.; Patil, S.A.; Patil, R.N. AC conductivity and magnetoelectric effect in $MnFe_{1.8}Cr_{0.2}O_4$-$BaTiO_3$ composites. *Mater. Sci. Eng. B Solid State Mater. Adv. Technol.* **2001**, *87*, 53–58. [CrossRef]
56. Gatos, K.G.; Apostolopoulos, N.; Patsidis, A.C.; Psarras, G.C. Effect of Carbonate Mineral Fillers on the Dielectric Properties and Fire Resistance of Polar and Non-Polar Halogen-Free Flame-Retardant Polymer Compounds. *J. Compos. Sci.* **2024**, *8*, 529. [CrossRef]
57. Yaqoob, S.; Ali, Z.; D'Amore, A. Magnetic and Dielectric Properties of Cobalt and Zirconium Co-Doped Iron Oxide Nanoparticles via the Hydrothermal Synthesis Approach. *J. Compos. Sci.* **2025**, *9*, 32. [CrossRef]
58. Tsyganov, A.; Morozova, N.; Vikulova, M.; Asmolova, A.; Artyukhov, D.; Zotov, I.; Gorokhovsky, A.; Gorshkov, N. The Effect of Lithium Doping on the Dielectric Properties of Solid Solutions $Li_xCa_{(1-x)}Cu_3Ti_4O_{12}$ (x = 0.01–0.1). *J. Compos. Sci.* **2023**, *7*, 282. [CrossRef]
59. Tayari, F.; Benamara, M.; Lal, M.; Essid, M.; Thakur, P.; Kumar, D.; Teixeira, S.S.; Graça, M.P.F.; Nassar, K.I. Exploring Enhanced Structural and Dielectric Properties in Ag-Doped $Sr(NiNb)_{0.5}O_3$ Perovskite Ceramic for Advanced Energy Storage. *Ceramics* **2024**, *7*, 958–974. [CrossRef]
60. Hizi, W.; Gassoumi, M.; Rahmouni, H.; Guesmi, A.; Ben Hamadi, N.; Dhahri, E. Effect of Sintering Temperature and Polarization on the Dielectric and Electrical Properties of $La_{0.9}Sr_{0.1}MnO_3$ Manganite in Alternating Current. *Materials* **2022**, *15*, 3683. [CrossRef]
61. Singh Yadav, R.; Kuřitka, I.; Vilcakova, J.; Jamatia, T.; Machovsky, M.; Skoda, D.; Urbánek, P.; Masař, M.; Urbánek, M.; Kalina, L.; et al. Impact of sonochemical synthesis condition on the structural and physical properties of $MnFe_2O_4$ spinel ferrite nanoparticles. *Ultrason. Sonochem.* **2020**, *61*, 104839. [CrossRef]
62. Sebastian, R.M.; Mohammed, E.M. Structural and electrical studies of Gd^{3+} substituted zinc ferrite nano particles. *Ferroelectrics* **2016**, *504*, 53–63. [CrossRef]
63. Daoudy, M.; Gouitaa, N.; Ahjyaje, F.Z.; Lamcharfi, T.-d.; Abdi, F. BZT substitution effect on the characteristics of (1 − x) MT − x BZT composite ceramics synthesized by the sol–gel method. *Arab. J. Chem.* **2024**, *17*, 105392. [CrossRef]
64. Lopes, T.J.; Azevedo, A.M.d.; Monteiro, S.N.; Araujo-Moreira, F.M. Electrical Properties of Composite Materials: A Comprehensive Review. *J. Compos. Sci.* **2025**, *9*, 438. [CrossRef]
65. Gouitaa, N.; Taj-Dine, L.; Farid, A.; Zahra, A.F. Structural, dielectric and electrical properties of modified $BaTi_{0.80}Fe_{0.20}O_3$ ceramics by Zr addition in Ti site at x = 0.00 to 0.10. *Iran. J. Mater. Sci. Eng.* **2021**, *18*, 1. [CrossRef]
66. Chen, Q.B.; Meng, B.; Zhao, M.Y.; Xie, H.; Bian, L.F.; Yang, X. Grain size effect on the electrical conductivity of submicron Sm-heavily-doped ceria. *Ceram. Int.* **2018**, *44*, 21507–21513. [CrossRef]
67. Chen, Y.; Tan, J.; Sun, J.; Guo, H.; Bai, J.; Zhou, P.; Zhang, D.; Liu, G. Effect of sintering temperature on the microstructures and mechanical properties of ZrO_2 ceramics fabricated by additive manufacturing. *Ceram. Int.* **2024**, *50*, 11392–11399. [CrossRef]
68. Efremov, V.V.; Korneikov, R.I.; Aksenova, S.V.; Zernov, Y.G.; Reznichenko, T.V.; Ivanov, N.P.; Azon, S.A.; Belov, A.A.; Fedorets, A.N.; Kravchenko, O.E.; et al. Advancements in $ZnFe_2O_4$ Synthesis: A Comparative Study of Sol–Gel and Solid-State Methods for Next-Generation Battery Applications. *J. Compos. Sci.* **2025**, *9*, 632. [CrossRef]
69. Slaoui, M.; Gouitaa, N.; Lahrichi, A.; Harrach, A.; Haddad, M.; Lamcharfi, T. Synthesis and physico-chemical characterization of solid solution (1 − x)ccto-xpbtio3. *Asian J. Chem.* **2021**, *33*, 1208–1214. [CrossRef]
70. Jafarpour, M.; Rostami, M.; Khalkhali, S.M.H.; Nikmanesh, H.; Majles Ara, M.H. The effect of lanthanum substitution on the structural, magnetic, and dielectric properties of nanocrystalline Mn-Ni spinel ferrite for radio frequency (RF) applications. *Phys. Lett. Sect. A Gen. At. Solid State Phys.* **2022**, *446*, 128285. [CrossRef]
71. Daoudy, M.; Gouitaa, N.; Ahjyaje, F.Z.; Lamcharfi, T.E.; Abdi, F. Synthesis, structural study, optical, dielectric, and electrical properties of a new lead-free $C_2H_5NH_3BaCl_3$ organic–inorganic hybrid perovskite. *J. Mater. Res.* **2024**, *39*, 1411–1424. [CrossRef]
72. Ravinder, D.; Seshagiri Rao, T.; Muley, V.N.; Reddy, K.B. Dependence of electrical conductivity and activation energy of lithium–zinc ferrites on sintering temperature and porosity. *Cryst. Res. Technol.* **1990**, *25*, 1475–1483. [CrossRef]
73. Jadhav, L.D.; Pawar, S.H.; Chourashiya, M.G. Effect of sintering temperature on structural and electrical properties of gadolinium doped ceria ($Ce_{0.9}Gd_{0.1}O_{1.95}$). *Bull. Mater. Sci.* **2007**, *30*, 97–100. [CrossRef]
74. Madhukar, N.P.; Gurukrishna, K.; Bhat, B.R.; Shanubhogue, U.D.; Mangavati, S.; Rao, A.; Chattopadhyay, S. Role of sintering temperature in modulating the charge transport of BiCuSeO thermoelectric system: Correlations to the microstructure. *Appl. Phys. A Mater. Sci. Process.* **2024**, *130*, 55. [CrossRef]
75. Alzahrani, B.; Hcini, S.; Mnefgui, S.; Dhahri, A.; Bouazizi, M. lamjed Sintering temperature effects on the impendence spectroscopy properties of $Nd_{0.67}Pb_{0.33}Mn_{0.9}Al_{0.1}O_3$ perovskites. *Phase Transit.* **2020**, *93*, 417–428. [CrossRef]
76. Wang, H.; Zhao, H.; Liang, W.; Fan, S.; Kang, J. Effect of sintering process on the electrical properties and microstructure of Ca-doped ZnO varistor ceramics. *Mater. Sci. Semicond. Process.* **2021**, *133*, 105880. [CrossRef]

77. Radu, I.; Turcan, I.; Lukacs, A.V.; Roman, T.; Bulai, G.A.; Olariu, M.A.; Dumitru, I.; Pui, A. Structural, dielectric and gas sensing properties of gadolinium (Gd^{3+}) substituted zinc-manganese nanoferrites. *Polyhedron* **2022**, *221*, 115893. [CrossRef]
78. Souri, M.; Salar Amoli, H. Gas sensing mechanisms in ABO_3 perovskite materials at room temperature: A review. *Mater. Sci. Semicond. Process.* **2023**, *156*, 107271. [CrossRef]
79. Bartolomé, J.; Taeño, M.; Martínez-Casado, R.; Maestre, D.; Cremades, A. Ethanol gas sensing mechanisms of p-type NiO at room temperature. *Appl. Surf. Sci.* **2022**, *579*, 152134. [CrossRef]
80. Tiemann, M. Porous Metal Oxides as Gas Sensors. *Chem. Eur. J.* **2007**, *13*, 8376–8388. [CrossRef] [PubMed]
81. Xu, C.; Tamaki, J.; Miura, N.; Yamazoe, N. Grain size effects on gas sensitivity of porous SnO_2-based elements. *Sens. Actuators B Chem.* **1991**, *3*, 147–155. [CrossRef]
82. Barsan, N.; Weimar, U. Conduction model of metal oxide gas sensors. *J. Electroceram.* **2001**, *7*, 143–167. [CrossRef]
83. Ponzoni, A.; Baratto, C.; Cattabiani, N.; Falasconi, M.; Galstyan, V.; Nunez-Carmona, E.; Rigoni, F.; Sberveglieri, V.; Zambotti, G.; Zappa, D. Metal Oxide Gas Sensors, a Survey of Selectivity Issues Addressed at the SENSOR Lab, Brescia (Italy). *Sensors* **2017**, *17*, 714. [CrossRef] [PubMed]
84. Gurlo, A. Nanosensors: Towards morphological control of gas sensing activity. SnO_2, In_2O_3, ZnO and WO_3 case studies. *Nanoscale* **2011**, *3*, 154–165. [CrossRef] [PubMed]
85. Baeumer, C.; Liang, A.Y.L.; Trstenjak, U.; Lu, Q.; Waser, R.; Mefford, J.T.; Gunkel, F.; Nemšák, S.; Chueh, W.C. Carbonate formation lowers the electrocatalytic activity of perovskite oxides for water electrolysis. *J. Mater. Chem. A* **2021**, *9*, 19940–19948. [CrossRef]
86. Fu, B.; Bi, L.; Lin, J.; Fu, J.; Wen, J.; Zou, B.; Wang, C.; Wang, Y. Low-temperature detection and excellent selectivity of ethanol using $LaFeO_3$ gas sensors with dual regulation of doping and non-stoichiometry. *J. Alloys Compd.* **2025**, *1013*, 178590. [CrossRef]